AD-A100 698 CALIFORNIA RESEARCH AND TECHNOLOGY INC WOODLAND HILLS F/G 18/3
STRESS WAVE INTERACTIONS WITH TUNNELS BURIED IN WELL-CHARACTERI--ETC(U)
JUN 80 M ROSENBLATT, L A DEANGELO DNA001-77-C-0203
UNCLASSIFIED CRT-3170F DNA-5334F NL

1 OF 1
AD
A100698

END
DATE
FILMED
7-81
DTIC

LEVEL II

(12)

DNA 5334F

STRESS WAVE INTERACTIONS WITH TUNNELS BURIED IN WELL-CHARACTERIZED JOINTED MEDIA

AD A100098

Martin Rosenblatt

Larry A. DeAngelo

California Research and Technology, Inc.

6269 Variel Avenue

Woodland Hills, California 91367

1 June 1980

Final Report for Period 4 May 1977—1 June 1980

CONTRACT Nos. DNA 001-77-C-0203
DNA 001-79-C-0278

APPROVED FOR PUBLIC RELEASE;
DISTRIBUTION UNLIMITED.

THIS WORK SPONSORED BY THE DEFENSE NUCLEAR AGENCY UNDER RDT&E RMSS CODES B344077464 Y99QAXSC06151 H2590D AND B344079464 Y99QAXSC06166 H2590D.

DDC FILE COPY

Prepared for
Director
DEFENSE NUCLEAR AGENCY
Washington, D. C. 20305

DTIC
JUN 1 0 1981
A

Destroy this report when it is no longer needed. Do not return to sender.

PLEASE NOTIFY THE DEFENSE NUCLEAR AGENCY, ATTN: STTI, WASHINGTON, D.C. 20305, IF YOUR ADDRESS IS INCORRECT, IF YOU WISH TO BE DELETED FROM THE DISTRIBUTION LIST, OR IF THE ADDRESSEE IS NO LONGER EMPLOYED BY YOUR ORGANIZATION.

NATIONAL PRINTING PLANT

UNCLASSIFIED

SECURITY CLASSIFICATION OF THIS PAGE (When Data Entered)

REPORT DOCUMENTATION PAGE

READ INSTRUCTIONS BEFORE COMPLETING FORM

1. REPORT NUMBER: DNA 5334F

2. GOVT ACCESSION NO: AD-A100 698

3. RECIPIENT'S CATALOG NUMBER:

4. TITLE (and Subtitle): STRESS WAVE INTERACTIONS WITH TUNNELS BURIED IN WELL-CHARACTERIZED JOINTED MEDIA

5. TYPE OF REPORT & PERIOD COVERED: Final Report ~~for period~~ 4 May 77 — 1 June 80

6. PERFORMING ORG. REPORT NUMBER: CRT-3170F

7. AUTHOR(s): Martin Rosenblatt, Larry A. DeAngelo

8. CONTRACT OR GRANT NUMBER(s): DNA 001-77-C-0203, DNA 001-79-C-0278

9. PERFORMING ORGANIZATION NAME AND ADDRESS: California Research & Technology, Inc., 6269 Variel Avenue, Woodland Hills, California 91367

10. PROGRAM ELEMENT, PROJECT, TASK AREA & WORK UNIT NUMBERS: Subtasks Y99QAXSC061-51, Y99QAXSC061-66

11. CONTROLLING OFFICE NAME AND ADDRESS: Director, Defense Nuclear Agency, Washington, DC 20305

12. REPORT DATE: 1 June 1980

13. NUMBER OF PAGES: 64

14. MONITORING AGENCY NAME & ADDRESS (if different from Controlling Office):

15. SECURITY CLASS. (of this report): UNCLASSIFIED

15a. DECLASSIFICATION DOWNGRADING SCHEDULE: N/A

16. DISTRIBUTION STATEMENT (of this Report): Approved for public release; distribution unlimited.

17. DISTRIBUTION STATEMENT (of the abstract entered in Block 20, if different from Report):

18. SUPPLEMENTARY NOTES: This work sponsored by the Defense Nuclear Agency under RDT&E RMSS Codes B344077464 Y99QAXSC06151 H2590D and B344079464 Y99QAXSC06166 H2590D.

19. KEY WORDS (Continue on reverse side if necessary and identify by block number):

Joints	Deeply Buried Structures
Block Motion	Numerical Simulation
Buried Tunnels	Computer Codes

20. ABSTRACT (Continue on reverse side if necessary and identify by block number):

For the DIABLO HAWK underground nuclear test, several small-scale tunnels were constructed in jointed rock simulant material and stress loaded to approximately 0.8 kbar = 11.6 ksi. These tunnel response tests represented an opportunity to evaluate whether successful pre-shot predictions of tunnel closure and block motion could be made for tunnels buried in a well-characterized jointed media. In this report, numerical simulation predictions using computer code techniques which explicitly treat the idealized joints —

DD FORM 1473 EDITION OF 1 NOV 65 IS OBSOLETE

UNCLASSIFIED

SECURITY CLASSIFICATION OF THIS PAGE (When Data Entered)

20. Abstract (continued)

are described and compared to data from the recovered experimental model. The tunnel closure predictions and the predicted locations of block motion are in reasonable agreement with some experimental data.

Other aspects of the study included:

- development and application of an analytical technique for predicting joint activation conditions (i.e., block motions) for specified joint orientations and locations near the tunnel surface,
- calculations and comparisons of tunnel response to dynamic and quasi-static stress loads, and
- investigation of the effects of joint friction on tunnel damage.

TABLE OF CONTENTS

Section		Page
	LIST OF ILLUSTRATIONS	2
1	INTRODUCTION AND SUMMARY	5
	1.1 BACKGROUND	5
	1.2 OBJECTIVE AND APPROACH	7
	1.3 SUMMARY AND CONCLUSIONS	9
	1.3.1 Joint Activation	9
	1.3.2 Dynamic Response Cases	13
	1.3.3 Quasi-Static Tunnel Response Prediction	13
2	JOINT ACTIVATION ANALYSIS	16
3	DYNAMIC RESPONSE CASES	29
	3.1 MATERIAL PROPERTIES	30
	3.2 CASE COMPARISONS FOR THE 0.8 KBAR DYNAMICALLY LOADED TUNNELS	32
	3.2.1 Effect of Loading Rise Time	32
	3.2.2 Effects of Rock Tensile Strength and Joint Shear Strength	35
4	DIABLO HAWK SMALL-SCALE STRUCTURE PREDICTION CASE	42
	4.1 PROBLEM CONFIGURATION	42
	4.2 QUASI-STATIC SOLUTION TECHNIQUE	42
	4.3 JOINT SLIDING	45
	4.4 TENSILE CRACKING	45
	4.5 TUNNEL CLOSURE AND COMPARISON WITH EXPERIMENTAL DATA	47
Appendix		
A	JOINT ACTIVATION CONDITIONS NEAR A CYLINDRICAL TUNNEL	53
	REFERENCES	58

LIST OF ILLUSTRATIONS

Figure		Page
1	Jointing Arrangement for Models Assembled from 16A Rock Simulant	6
2	Joint Activation Stress Loads for Various Joint Orientations (α) as a Function of Tunnel Angle (β) for Constitutive Property Case P1 (τ_o = .04 kbar, ϕ = 33°, ν = .25) (Joints will be activated for all conditions in shaded area). . . .	10
3	Regions of Possible Joint Activation for a .5 kbar Stress Load Interacting with Joint Oriented at α = 0°, 45°, 90°, and ±45°. (Case P1, τ_o = .04 kbar, ϕ = 33°, ν = .25)	12
4	Comparison of Experimental Data and Prediction for the Tunnel Closure ($\Delta D/D$) versus Tunnel Angle for the Small-Scale DIABLO HAWK Model S-D1-2-5. . .	15
5	Static Tangential Stress Field (σ_2) from a Planar Loading Wave (σ_{load}) as a Function of Tunnel Angle (β) for Two Values of Poisson's Ratio (ν)	18
6	Joint Activation Stress Loads for Various Joint Orientations (α) as a Function of Tunnel Angle (β) for Constitutive Property Case P2 (τ_o = .08, ϕ = 33°, ν = .25)	20
7	Joint Activation Stress Loads for Various Joint Orientations (α) as a Function of Tunnel Angle (β) for Constitutive Property Case P3 (τ_o = .02, ϕ = 33°, ν = .25)	21
8	Joint Activation Stress Loads for Various Joint Orientations (α) as a Function of Tunnel Angle (β) for Constitutive Property Case P4 (τ_o = .04, ϕ = 0°, ν = .25).	22
9	Joint Activation Stress Loads for Various Joint Orientations (α) as a Function of Tunnel Angle (β) for Constitutive Property Case P5 (τ_o = .04, ϕ = 33°, ν = .4).	23

LIST OF ILLUSTRATIONS (continued)

Figure		Page
10	Regions of Possible Joint Activation for a Variation in Joint Cohesion, τ_o (σ_{load} = .5 kbar)	24
11	Regions of Possible Joint Activation for a Variation in Joint Cohesion, τ_o (σ_{load} = .5 kbar)	25
12	Regions of Possible Joint Activation for a Variation of Friction Angle, ϕ (σ_{load} = .5 kbar)	26
13	Regions of Possible Joint Activation for a Variation in Poisson's Ratio, ν (σ_{load} = .5 kbar)	27
14	Particle Velocity and Principal Stress Fields at 62 μsec for the Elastic-Plastic Media Model (Case 1, 0.8 kbar Loading in 100 μsec)	34
15	Tensile Stress versus Time at the Tunnel Crown for Various Stress Wave Rise Times (t_r) to a Maximum Load of 0.8 kbar	36
16	Treatment of Tensile Cracks in WAVE-L Code	37
17	Tensile Crack Configuration at t = 55 μsec for Tensile Strength of 100 psi and 500 psi (Cases 4 and 5; 0.8 kbar = 11.6 ksi Stress Loading in 100 μsec)	39
18	Tensile Crack Configuration at t = 127 μsec for Tensile Strength of 100 psi and 500 psi (Cases 4 and 5; 0.8 kbar = 11.6 ksi Stress Loading in 100 μsec)	40
19	Tensile Crack Configuration at t = 127 μsec for a Variation of Friction (Case 6) versus Frictionless (Case 5) Joints (0.8 kbar = 11.6 ksi Stress Loading in 100 μsec)	41
20	Initial Conditions and Computational Grid for the Joints Being Perpendicular to the Wave Vector (Using WES Material Properties)	43

LIST OF ILLUSTRATIONS (continued)

Figure		Page
21	Successive Steps in Quasi-Static Numerical Simulation Technique.	44
22	Slide Displacement Along the Various Joints versus Distance Along the Joint for Quasi-Static Calculation of a Small-Scale Model in DIABLO HAWK .	46
23	Final Tensile Crack Pattern from Quasi-Static Calculation of Small-Scale Model in DIABLO HAWK . .	48
24	Comparison of Experimental Data and Prediction for the Tunnel Closure ($\Delta D/D$) versus Tunnel Angle for the Small-Scale DIABLO HAWK Model S-D1-2-5. . .	49
25	Post-Shot Experimental Model S-D1-2-5	50
A-1	Mohr Diagram Relating the Shear Stress (τ) and Normal Stress (σ_n) for a Typical Stress State which Satisfies the Incipient Joint Slippage Criteria at $\phi = \psi_1$ and $\phi = \psi_2$	57

LIST OF TABLES

Table		Page
1	Tunnel Angles (β) for Minimum Loading Stress for Various Joint Orientations (α).	11
2	Joint and Earth Media Constitutive Properties . . .	19
3	The Dynamic Loading Cases	33

SECTION 1

INTRODUCTION AND SUMMARY

1.1 BACKGROUND

All rock masses contain large numbers of planar discontinuities or joints. These joints often react to an applied stress quite differently than the surrounding material and there is both experimental (Ref. 1) and theoretical (Refs. 2, 3) evidence to suggest that sliding motion across these joints should be one of the important considerations involved in designing underground structures which are to survive nuclear and/or conventional explosions.

In the recent DIABLO HAWK underground nuclear test, SRI International fielded several laboratory-scale structures in jointed rock simulant (Ref. 4). Figure 1 shows the general model designs. The jointed rock models are 18" and 30" in diameter, with 3" and 5" diameter tunnels, respectively. The SRI small-scale jointed structures experiment provides an opportunity for examining the influence of highly idealized jointed arrays on tunnel closure and damage characteristics.

There are both continuum and explicit approaches for predicting tunnel closure and damage in jointed media. In the continuum approach, the overall mechanical properties of the field are synthesized from the properties of the intact rock and the properties and arrangement of the joints; for example, stiffnesses and strengths used in the continuum model are lower than the intact rock properties. In the explicit approach, the properties and arrangement of individual blocks and joints are individually and explicitly modeled and used to calculate tunnel response to loading. Both of these treatments have important limitations: The rationale for choosing a set of degraded

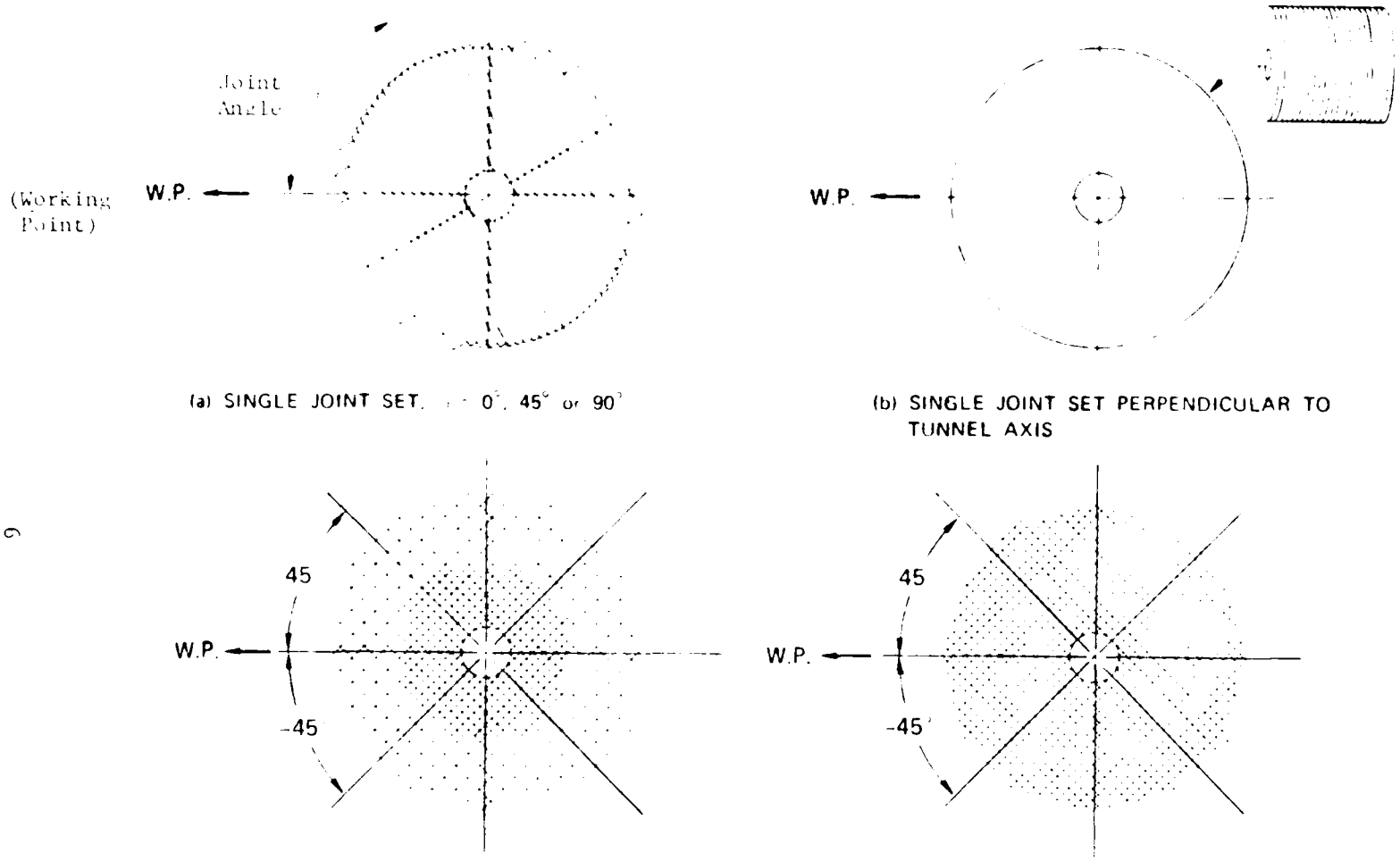

(a) SINGLE JOINT SET, 0°, 45° or 90°

(b) SINGLE JOINT SET PERPENDICULAR TO TUNNEL AXIS

(c) DOUBLE ORTHOGONAL JOINT SETS WITH COARSE JOINT SPACING IN OUTER ANNULUS ALSO FIELDED WITH JOINTS ORIENTED AT 0° AND 90° TO W.P

(d) DOUBLE ORTHOGONAL JOINT SETS WITH UNIFORM JOINT SPACING

Figure 1. JOINTING ARRANGEMENT FOR MODELS ASSEMBLED FROM 16A ROCK SIMULANT

The models shown have a nominal diameter of 18 inches with a 3-inch diameter tunnel. Some models will be 30 inches in diameter with a 5-inch diameter tunnel. (From Reference 4.)

properties in the continuum approach is usually hard to justify, and this approach precludes discontinuities in displacements across joints, which may be a critical omission. The properties of joints in the explicit approach are hard to measure, and the arrangement of joints in a real field around a real tunnel can only be estimated.

1.2 OBJECTIVE AND APPROACH

The objective of this study is to examine the influence of the joints on tunnel closure and damage using numerical techniques which explicitly treat the idealized joints in the SRI structure.

The approach involves three related aspects:

1. Joint Activation.

   An analytical closed form solution is derived for the initiation or activation of relative motion across a joint. The joint activation depends on (a) the relative orientation of the joint and the tunnel surface intersected by the joint, (b) the magnitude and propagation direction of the stress wave encompassing the tunnel, and (c) the shear stress on the joint which must exceed a critical value which depends on the normal stress across the joint as well as on surface roughness.

   In Section 2, the joint activation solution is derived and applied to the SRI small-scale models to estimate (a) the areas on the tunnel surface where joint activation is likely to occur, (b) the stress levels which are necessary to activate joints of various orientations, and (c) the sensitivity of joint activation to material properties.

2. Dynamic Tunnel Response Cases.

In the SRI small-scale models with tunnel diameters of 3", the transit time across this characteristic dimension is only 22 μsec in the 16A rock simulant material. Thus, since the rise times to peak stresses of ~0.8 kbar in the DIABLO HAWK event are ~5-10 msec, these small-scale structures are actually loaded (and unloaded) in a quasi-static fashion. Full-scale tunnels may be loaded more dynamically, therefore the effects of dynamic loading on small-scale tunnels buried in jointed media are analyzed using six plane strain computer code simulations with dynamic loading times of 100-400 μsec. These cases also vary the assumed joint and tensile strength properties of the rock simulant. The WAVE-L Lagrangian code is used; the basic formulation is similar to the HEMP code (Ref. 5). The numerical solutions and material properties are described in Section 3.

3. Quasi-Static Tunnel Response Prediction For a Small-Scale Structure Loaded to 0.8 kbar During the DIABLO HAWK Event.

A numerical simulation prediction of tunnel closure and damage is made and compared with a fielded small-scale SRI model (the model has a 3" tunnel diameter with ½" joint spacings, model # [illegible]).

The quasi-static solution technique and the calculational-experimental comparisons are described in Section 4.

1.3 SUMMARY AND CONCLUSIONS

1.3.1 Joint Activation

Although the response of a tunnel in a jointed medium must be solved numerically, the conditions that will <u>initiate joint slipping</u> can be analyzed in closed form if we assume an elastic media with joints, and a far field stress state of uniaxial strain with a stress loading of σ_{load}.

Figure 2 shows the loading stress (σ_{load}) required to activate a joint oriented at α = 0, ±45°, and 90° as a function of the angle (β) where the joint intersects the tunnel surface. Thus a joint oriented at α = 45° will require a loading stress of .06 kbar (900 psi) to become activated if this joint intersects the tunnel surface at β = 100° (see the following sketch and Figure 2).

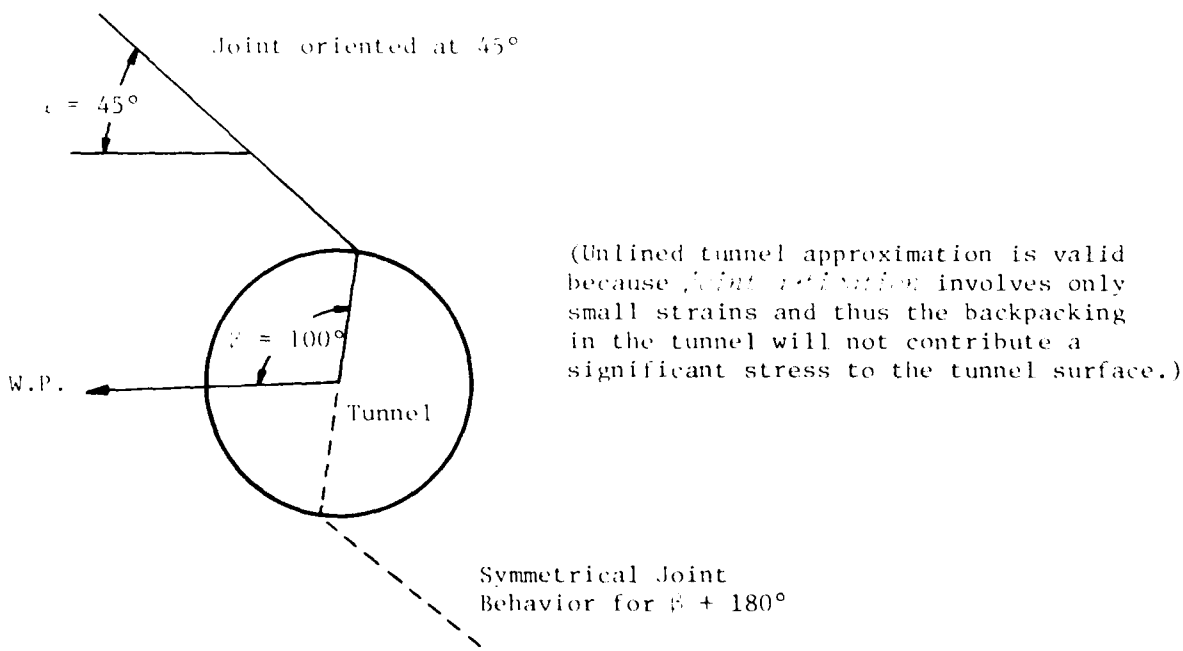

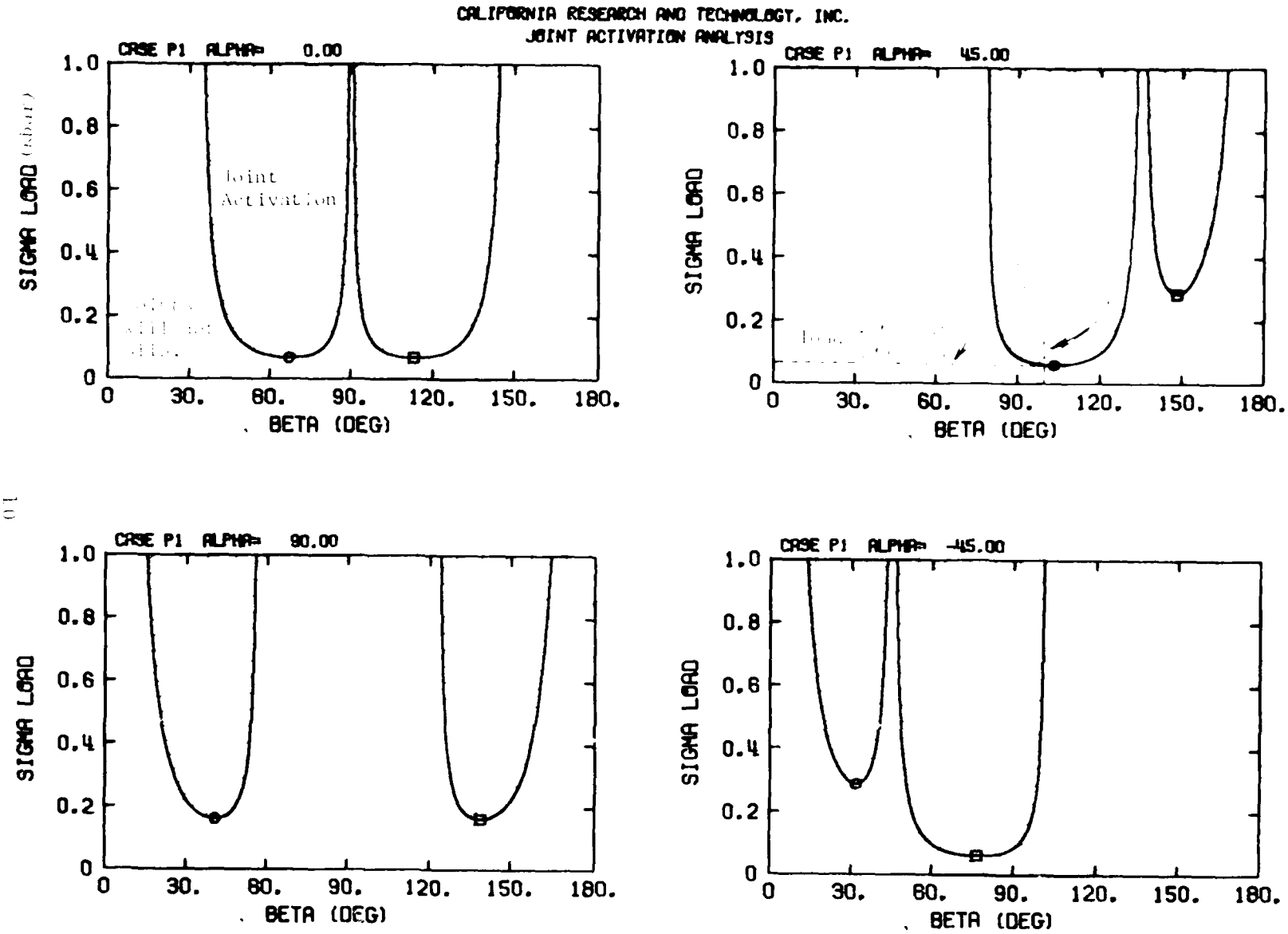

Figure [illegible] [illegible] Load for Various Joint Orientations ( ) as a function of [illegible] for [illegible] Property Case P1 ($_0$ = .04 kbar, = 33°, = .25)
([illegible] will be activated for all conditions in shaded areas)

Note that for each joint orientation (α), the shaded region on Figure 2 shows the angles (θ) on the tunnel surface where joint activation is possible as a function of loading stress (σ_{load}). Note that symmetry implies equivalent tunnel behavior at angles of θ + 180°. Joints will not slip outside of these shaded regions. The tunnel angles, θ, associated with absolute minimums in loading stress (σ_{load}) necessary for joint activation are indicated in Table 1. However, note that the activation stress curves (Figure 2) are relatively flat bottomed; and therefore, joint activation can occur over a fairly wide range in tunnel angles with only a small increase in loading.

Table 1. Tunnel Angles (θ) for Minimum Loading Stress for Various Joint Orientations (α).

Joint Orientation	Tunnel Angles for Minimum Loading Stress*		
α degree	θ degree	σ_{load} kbar	σ_{load} psi
0	67, 113	.068	986
45	103	.059	856
90	41, 139	.162	2350
45	76, 103	.059	856

*Representative constitutive properties are used (Case P1): Joint Cohesion (τ_0)=.04 kbar, Friction Angle (ϕ)=33°, Material Poisson's Ratio (ν)=.25.

Figure 3 shows the areas on the tunnel surface where joint activation (for a single joint) could occur for σ_{load} = .5 kbar.

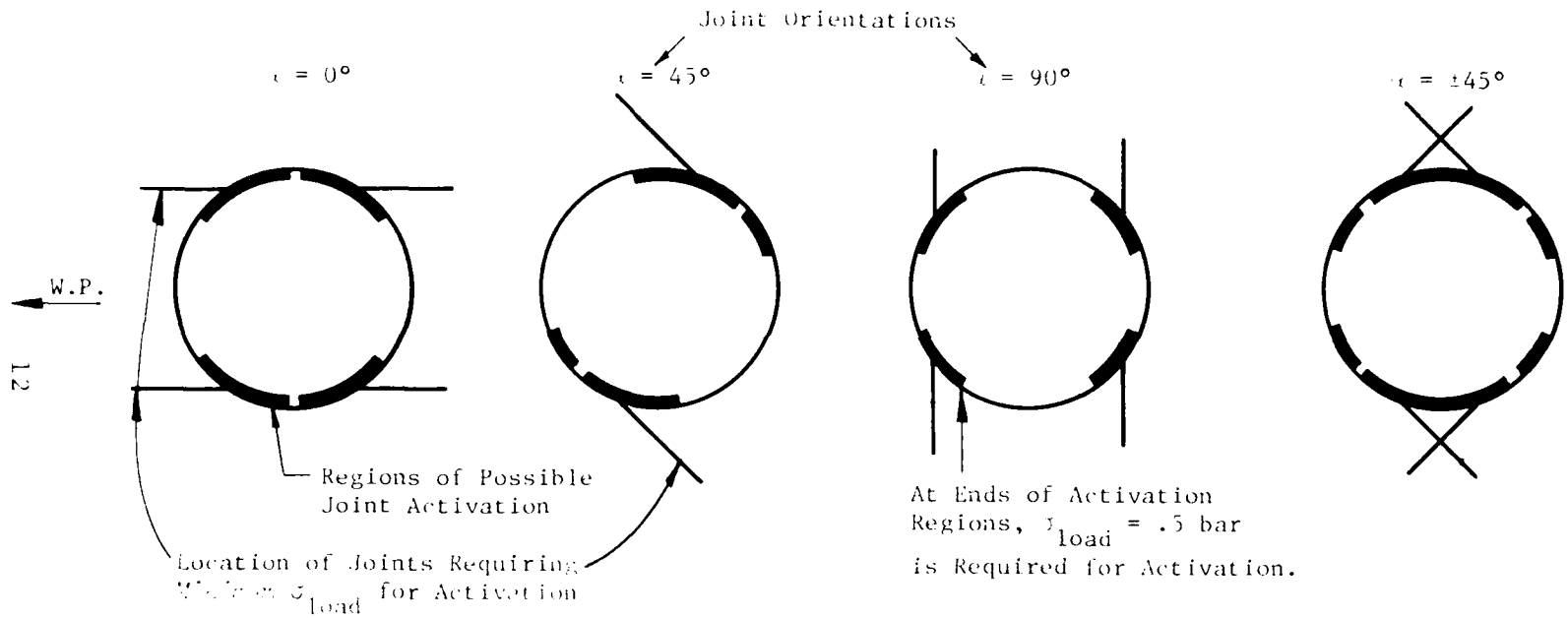

Figure 3. Regions of Possible Joint Activation for a .5 kbar Stress Load Interacting with Joint Oriented at α = 0°, 45°, 90°, and ±45°. (Case P1, σ_o = .04 kbar, φ = 33°, μ = .25)

All the joint orientations in the SRI experiment are shown for a representative set of joint and earth media properties. (Variations in the joint and earth media constitutive properties are illustrated in Section 2.)

1.3.2 Dynamic Response Cases

Six WAVE-L numerical simulations (Table 3) were performed involving 100-400 μsec stress rise times to a peak loading stress of 0.8 kbar on the SRI 3" diameter models. The wave transit time across the 3" tunnel opening is ~22 μsec, therefore, the dynamic tunnel response characteristics could be investigated.

The tensile stress history near the tunnel crown is strongly dependent on the stress wave rise time for times corresponding to a few transit times across the tunnel diameter. A stress wave rise time of 100 μsec (~5 transit times) caused a peak tensile stress of almost 150 bars. In the quasi-static loading case without joint slipping, no tensile stress developed near the crown.

[illegible] of the material near the tunnel surface is also related to the relative displacements* across the joints. When slipping occurs across joints, the plates of rock separated by the joints can act as unsupported beams due to the presence of the unlined tunnel. The resulting beam bending can lead to tensile stresses and fracture.

1.3.3 Quasi-Static Tunnel Response Prediction

The quasi-static solution technique is described in Section 4. Numerical simulation predictions using this technique were made for a fielded small-scale (3" diameter tunnel) SRI model. The

*The relative displacement or slipping across a joint is measured by the current distance between two points which were initially touching each other on opposite faces of the joint.

calculation predictions were made prior to excavation and examination of the model.

Figure 4 shows a comparison of the predicted tunnel closure (as a % of the diameter) versus tunnel angle, β. The agreement is reasonable except near the crown-invert (β = 0° and 180°). The maximum predicted closure is 1.2% at β = 30°. The experimental data show a maximum 1.6% closure at the crown-invert compared to a 0.5% predicted value at the crown-invert. This difference may be due to the moderate sliding on the joints and associated tensile failure and relaxation which occurs in the calculation, but not in the experiment.

In the post-shot experimental model, there was deformation of a thin (.003 inch) stainless steel tunnel liner which surrounds the foam filler. This liner may have inhibited sliding along the joints. The observed liner deformation is associated with the joints which are predicted to slide the most; thus, some "block motion" appears to have occurred.

It is concluded that tunnel closure in a well-characterized jointed media could be predicted using existing computer code techniques involving explicit descriptions of joint locations, orientations, and friction properties. Also, because of the important role joint (and fault) motion plays in determining damage to tunnel liners and nearby earth material, it is felt that continuum approaches to predicting tunnel closure and damage might not be as useful.

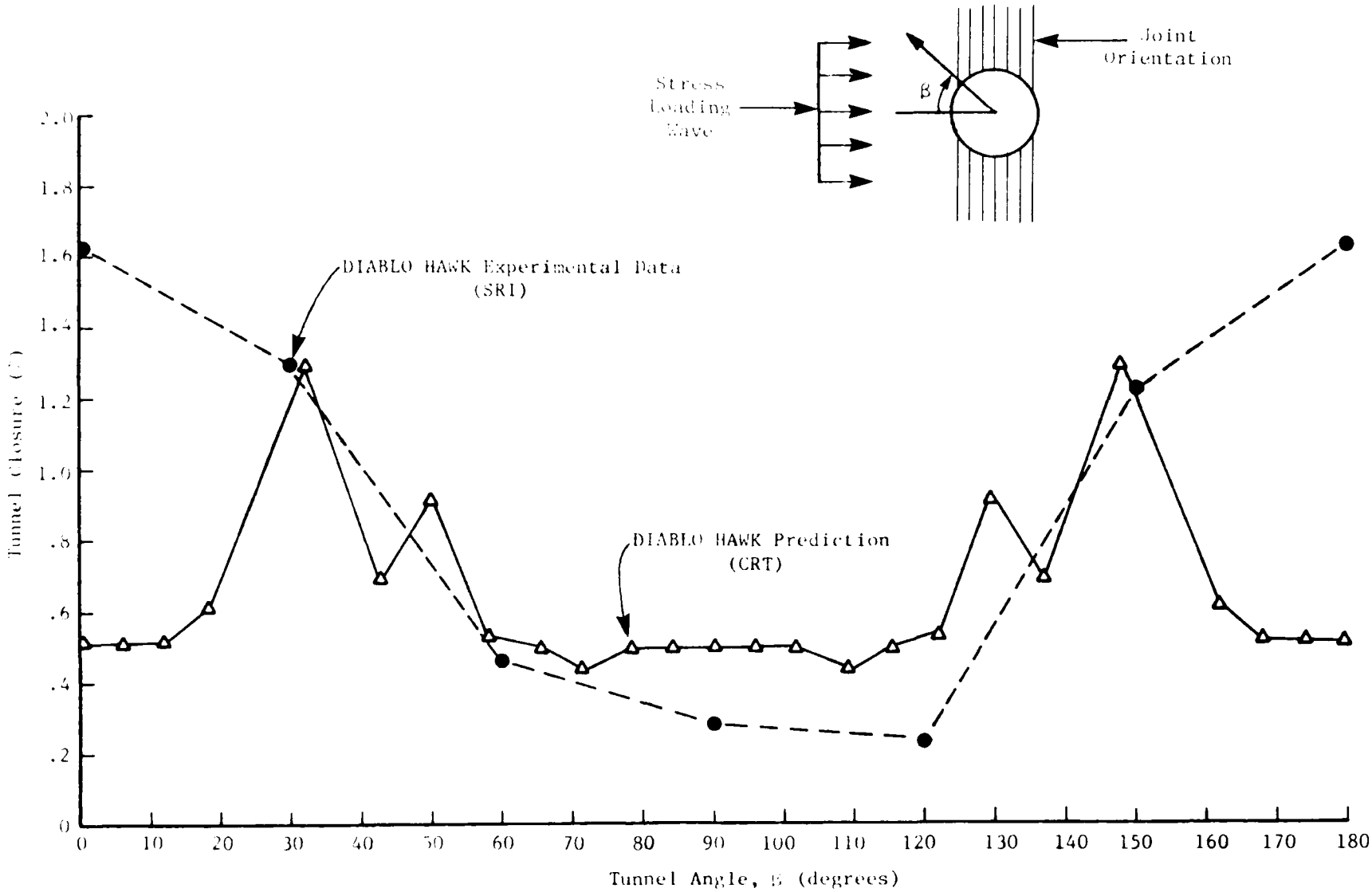

Figure 4. Comparison of Experimental Data and Prediction for the Tunnel Closure ($\frac{\Delta D}{D}$) versus Tunnel Angle for the Small-Scale DIABLO HAWK Model S-DI-2-5.

SECTION 2

JOINT ACTIVATION ANALYSIS

The necessary conditions for a joint or block to begin slipping depend on the relative orientation of the joint, the tunnel surface, and the stress wave, as indicated in the following sketch:

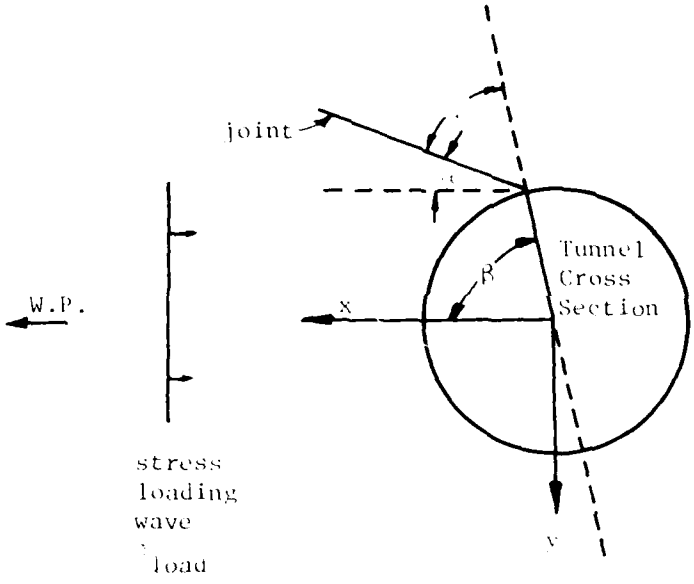

is the joint orientation angle

is the tunnel angle (angle where joint intersects tunnel)

is the angle between the joint and the normal to the tunnel surface,

Joint slippage will occur when the shear stress (τ) on the joint exceeds a critical value, τ_{max}. This value depends on the normal stress (σ_n) across the joint as well as on the surface roughness. Prior to joint activation, the earth media around the tunnel is assumed to respond elastically and statically to a uniaxial strain load from a (quasi-static) planar wave.

The key characteristics of interest, with respect to *joint activation* are:

- the areas on the tunnel surface where joint activation is likely to occur,
- the stress levels which are necessary to activate joints of various orientations,
- the sensitivity of joint activation to material properties.

The determination of these characteristics involves the following elements:

1. The *static tangential stress* field on the unlined tunnel surface (this stress field is shown in Figure 5 as a ratio with the loading stress, i.e., $\sigma_\beta/\sigma_{load}$).
2. The *joint constitutive model* (i.e., we assume $\tau_{max} = \tau_o + (\tan\phi)\sigma_n$ where τ_o and ϕ are experimentally determined parameters).
3. The *far field stress load* (σ^a_{load}) *for joint activation* as a function of joint orientation (α), position on the tunnel (β), and material properties.

The activation stress load relationship (derived in Appendix A) is

$$\sigma^a_{load} = \frac{(2\tau_o\cos\phi)/(\sin(2\psi-\phi) - \sin\phi)}{2 - [1 + 2\cos(2\beta)]\,\frac{[1-2\nu]}{[1-\nu]}} \qquad (1)$$

where

$\psi = |\alpha-\beta|$ (see sketch on previous page)

τ_o and ϕ are joint constitutive parameters

ν is the Poisson's Ratio for the earth material

$$A(\beta) = \frac{\sigma_2}{\sigma_{load}} = 2 - [1 + 2\cos(2\beta)] \left\{\frac{1-2\nu}{1-\nu}\right\}$$

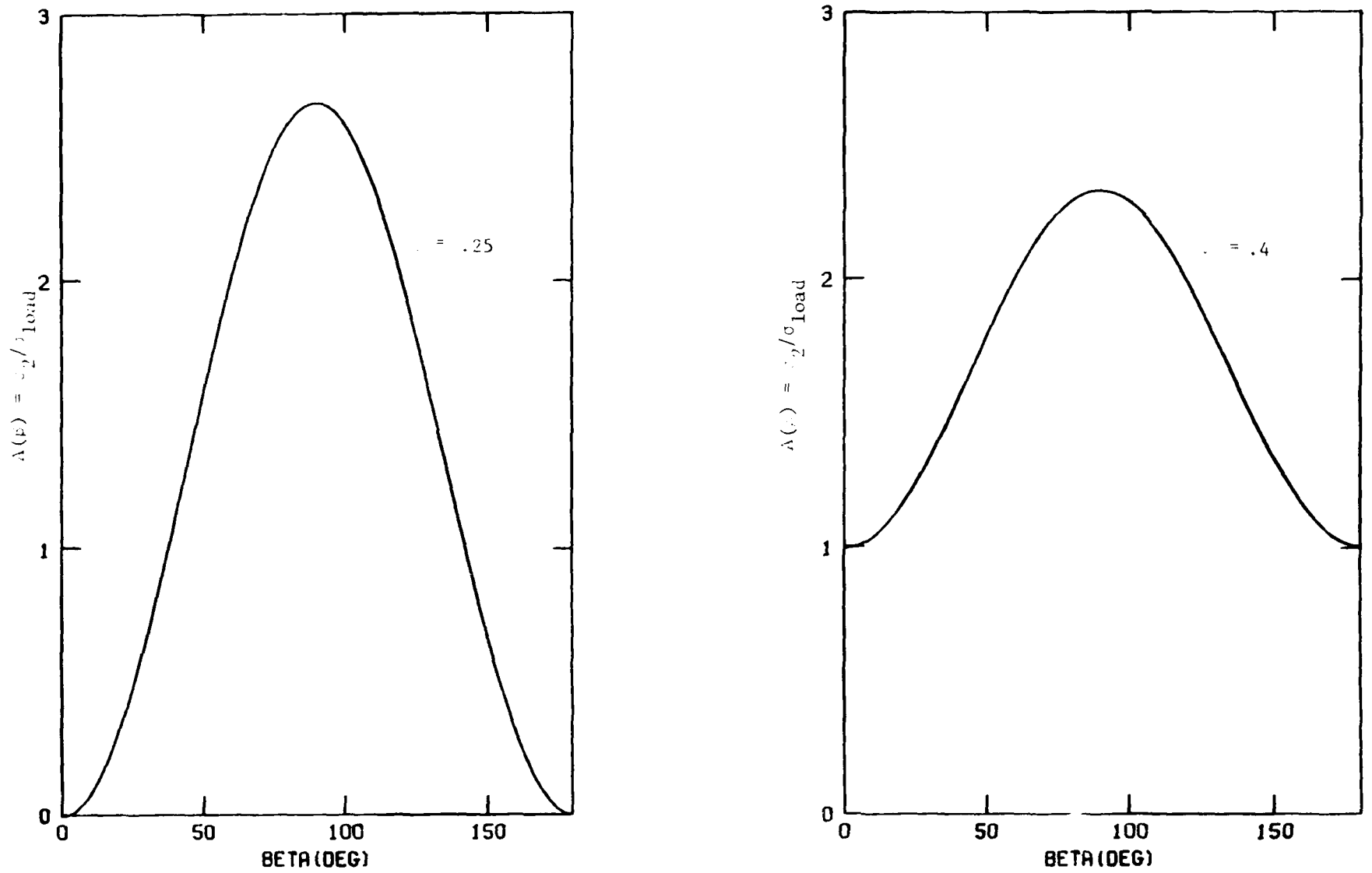

Figure 5. Static Tangential Stress Field (σ_2) from a Planar Loading Wave (σ_{load}) as a Function of Tunnel Angle (β) for Two Values of Poisson's Ratio (ν).

Note that Equation 1 shows that τ_o, ϕ, and ν are the constitutive properties of interest for joint activation. Table 2 lists the numerical values of these properties which were used to calculate joint activation relationships.

Table 2. Joint and Earth Media Constitutive Properties

Joint				Earth Media
Case	Cohesion*, τ_o kbar	Cohesion*, τ_o psi	Friction Angle* ϕ (degrees)	Poisson's Ratio ν
P1	.04	580	33	.25
P2	.08	1160	33	.25
P3	.02	290	33	.25
P4	.04	580	0	.25
P5	.04	580	33	.40

*The joint cohesion (τ_o) and friction angle (ϕ) are related to the unconfined compressive strength (σ_u) of the earth media by

$$\sigma_u = \frac{2\tau_o \cos\phi}{1 - \sin\phi}$$

Figure 2 and Figures 6 to 9 show the variations in σ_{load} versus tunnel angle (θ) for the joint and earth media property variations indicated in Table 2. Figure 3 and Figures 10 to 13 show the corresponding regions on the tunnel surface where joint activation is possible for σ_{load} = .5 kbar.

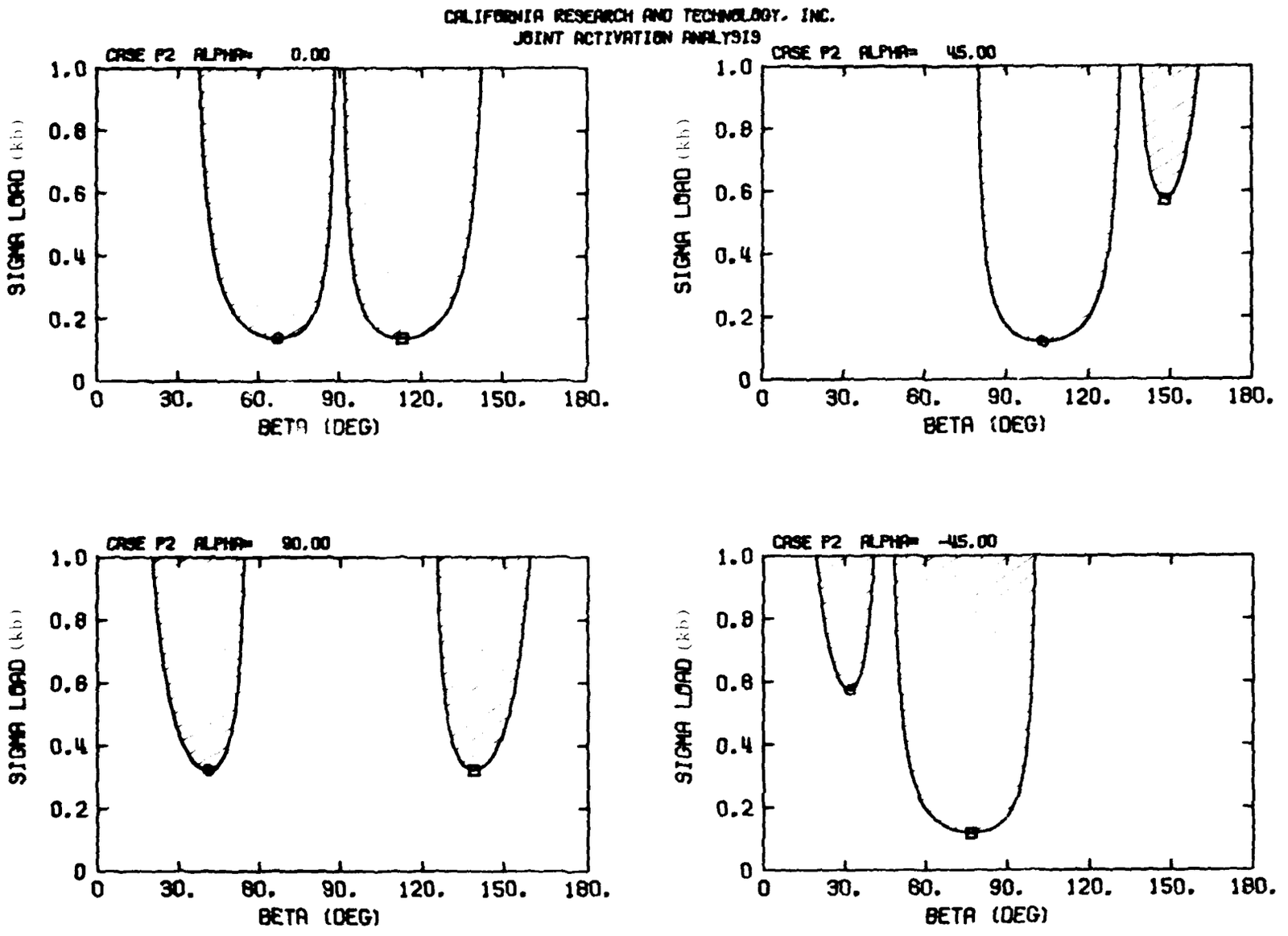

Figure 6. Joint Activation Stress Loads for Various Joint Orientations (α) as a Function of Tunnel Angle (β) for Constitutive Property Case P2 (ε_0=.08, ϕ=33°, ν=.25).

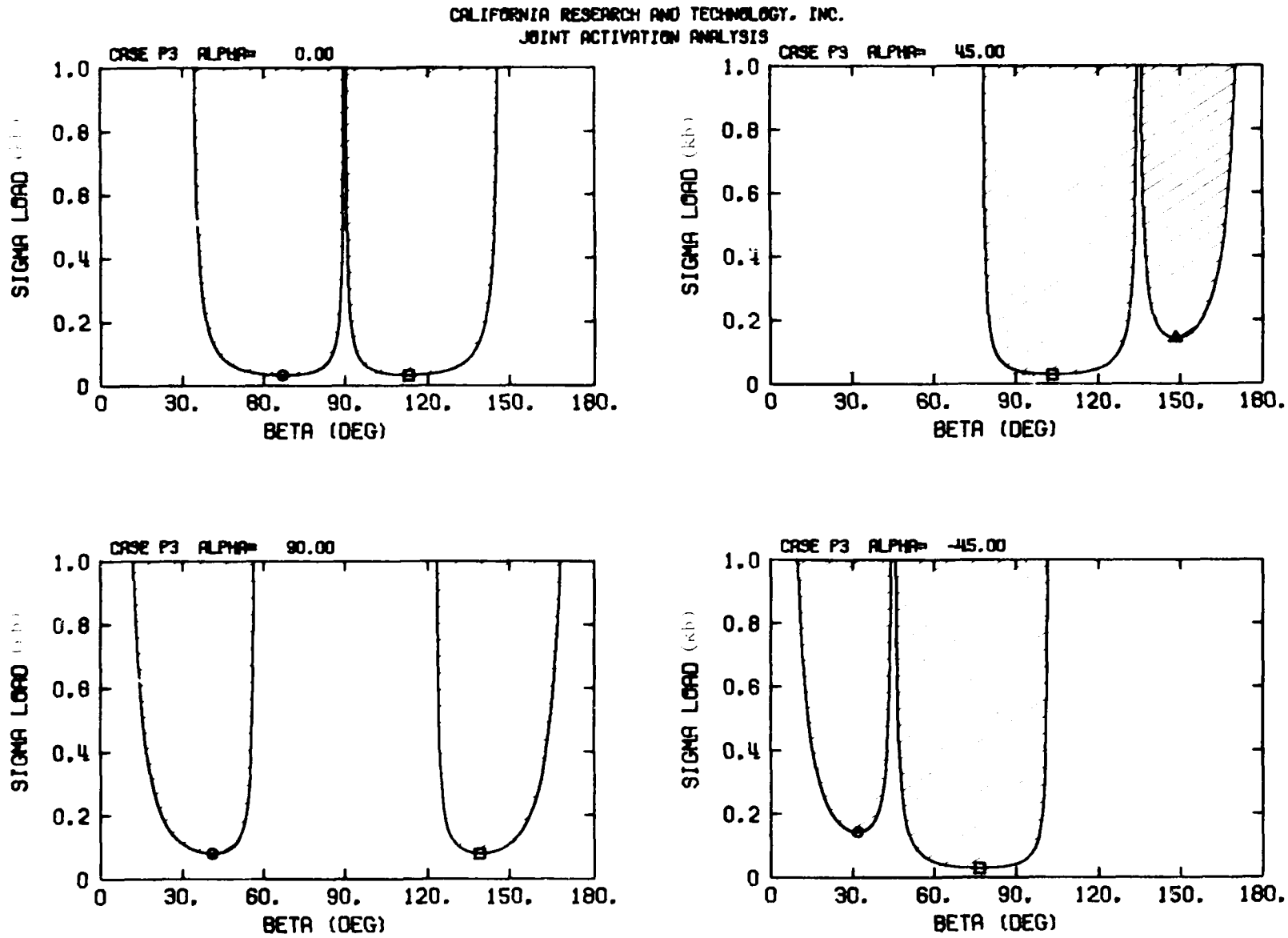

Figure 7. Joint Activation Stress Loads for Various Joint Orientations (α) as a Function of Tunnel Angle (β) for Constitutive Property Case P3 (ε_0=.02, ϕ=33°, μ=.25).

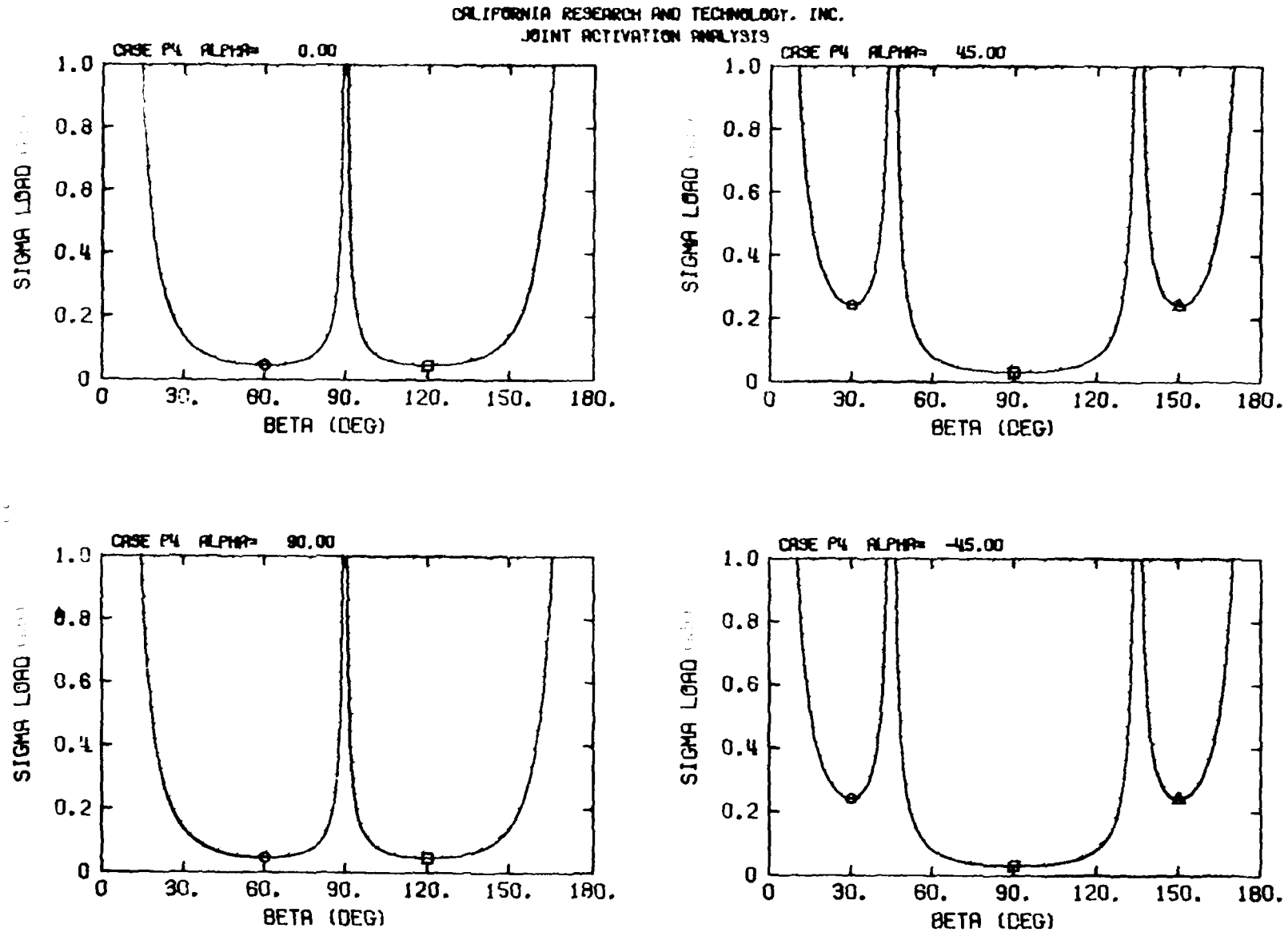

Figure [illegible]. Joint Activation Stress Loads for Various Joint Orientations ([illegible]) as a Function of Tunnel Angle ( ) for Constitutive Property Case P4 ([illegible]=.04 [illegible], [illegible] , [illegible].25)

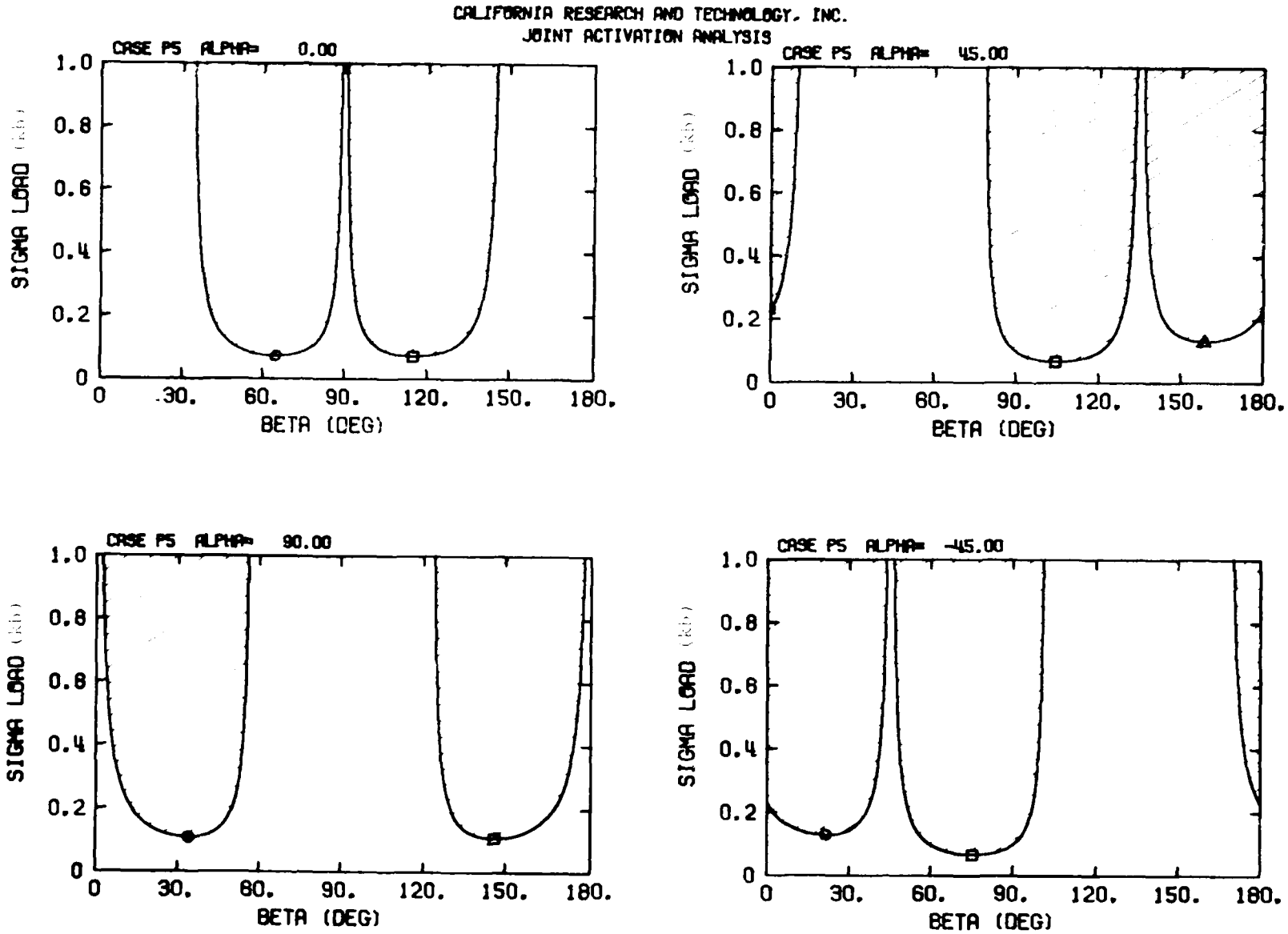

Figure 4. Joint Activation Stress Loads for Various Joint Orientations (α) as a Function of Tunnel Angles (β) for Constitutive Property Case P5 (τ_0 = .04 kbar, ϕ=33°, =.4)

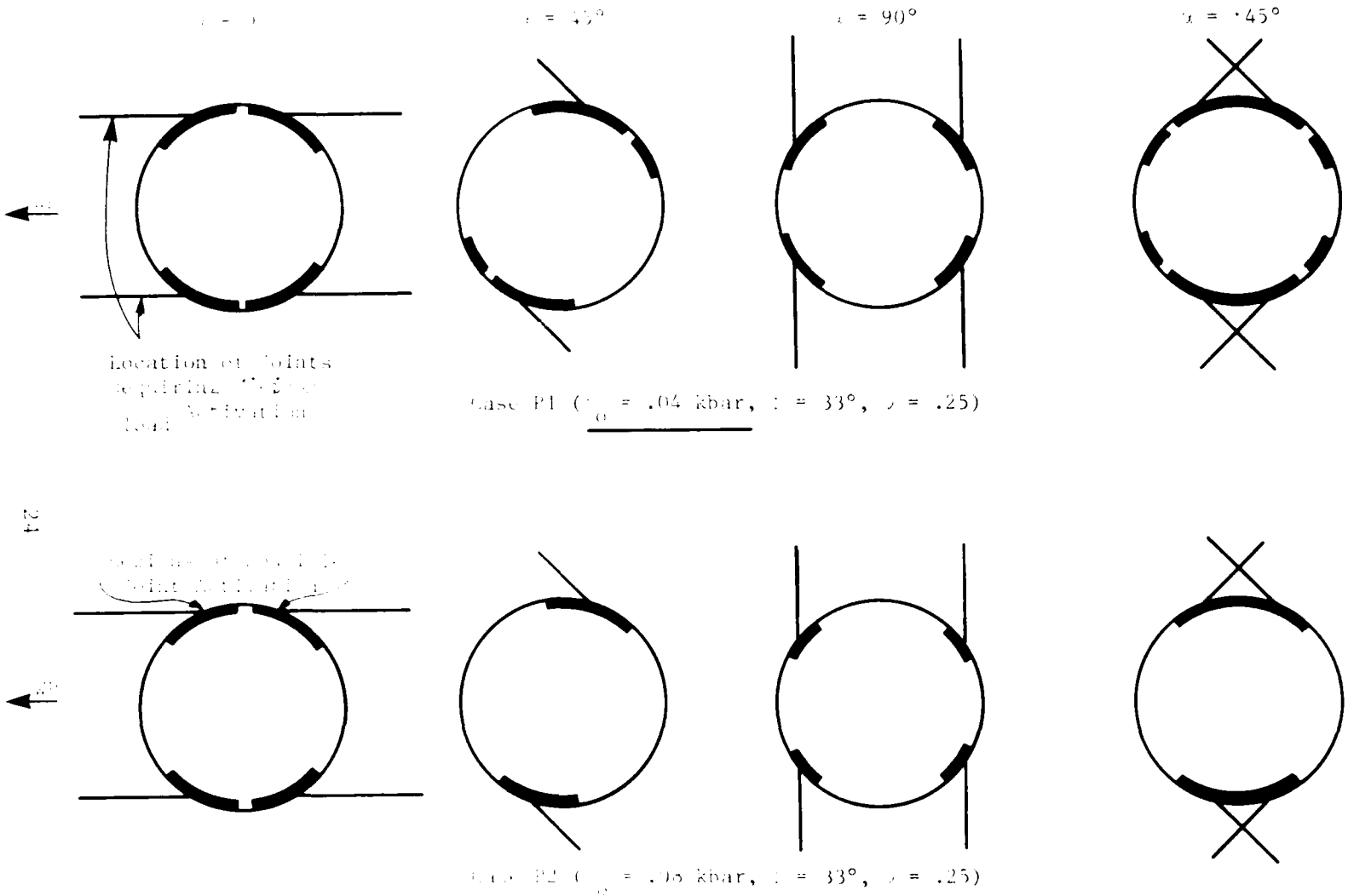

Figure [illegible]. Regions of Possible Joint Activation for a Variation in Joint Cohesion, σ_o (σ_{load} = .5 kbar).

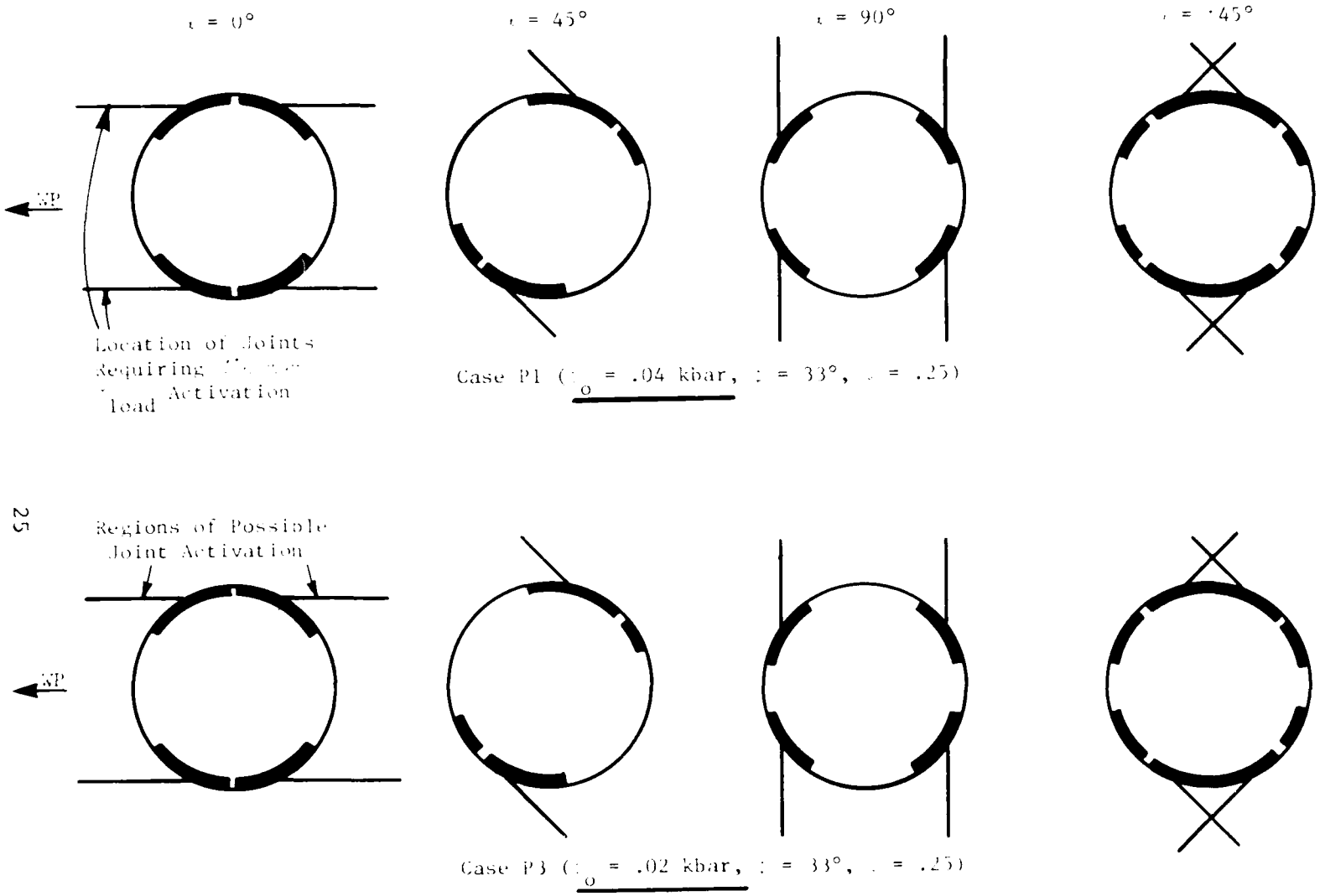

Figure 11. Regions of Possible Joint Activation for a Variation in Joint Cohesion, τ_o (τ_{load} = .5 kbar).

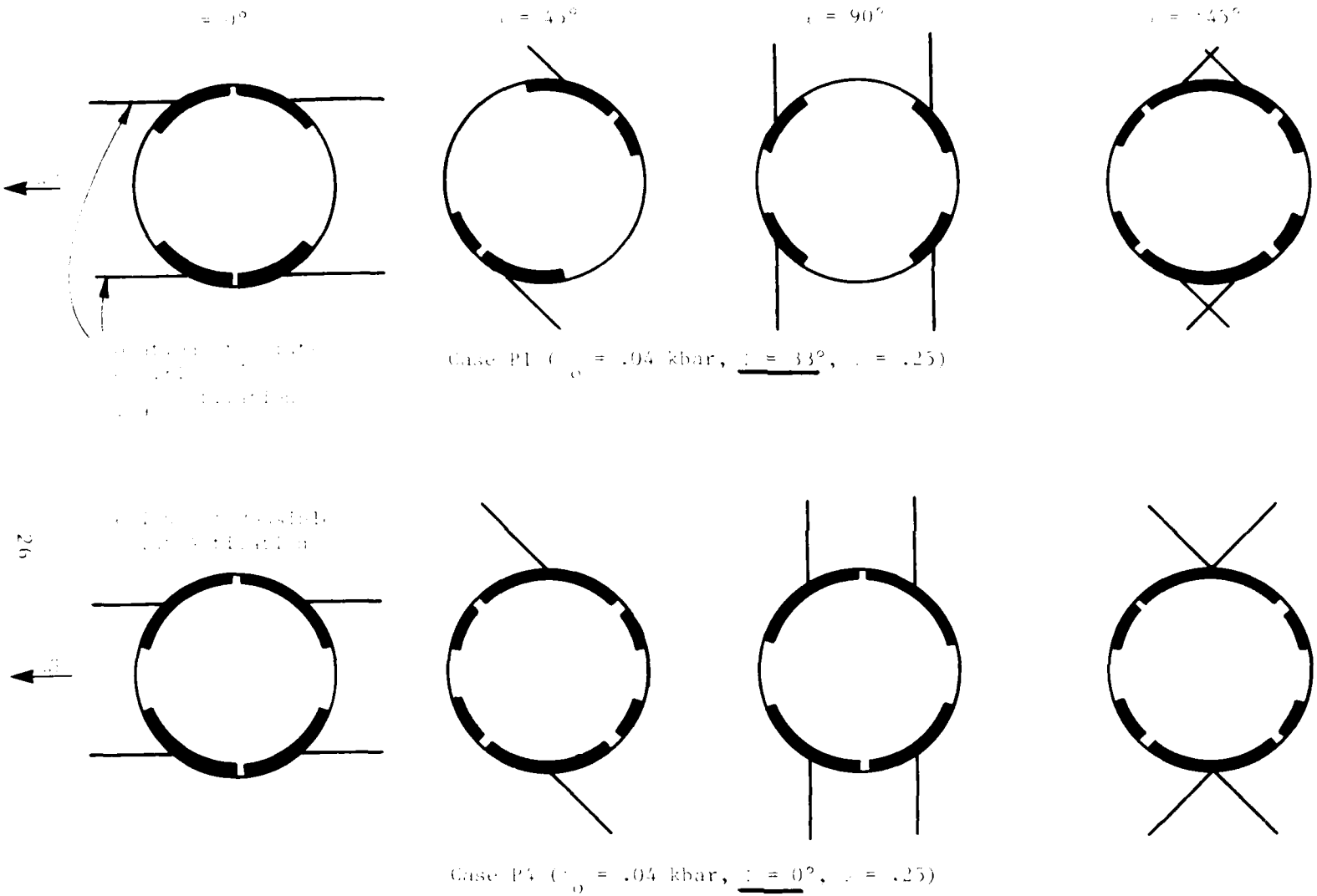

Figure 12. Regions of Possible Joint Activation for a Variation of Friction Angle, ϕ (σ_{load} = .5 kbar).

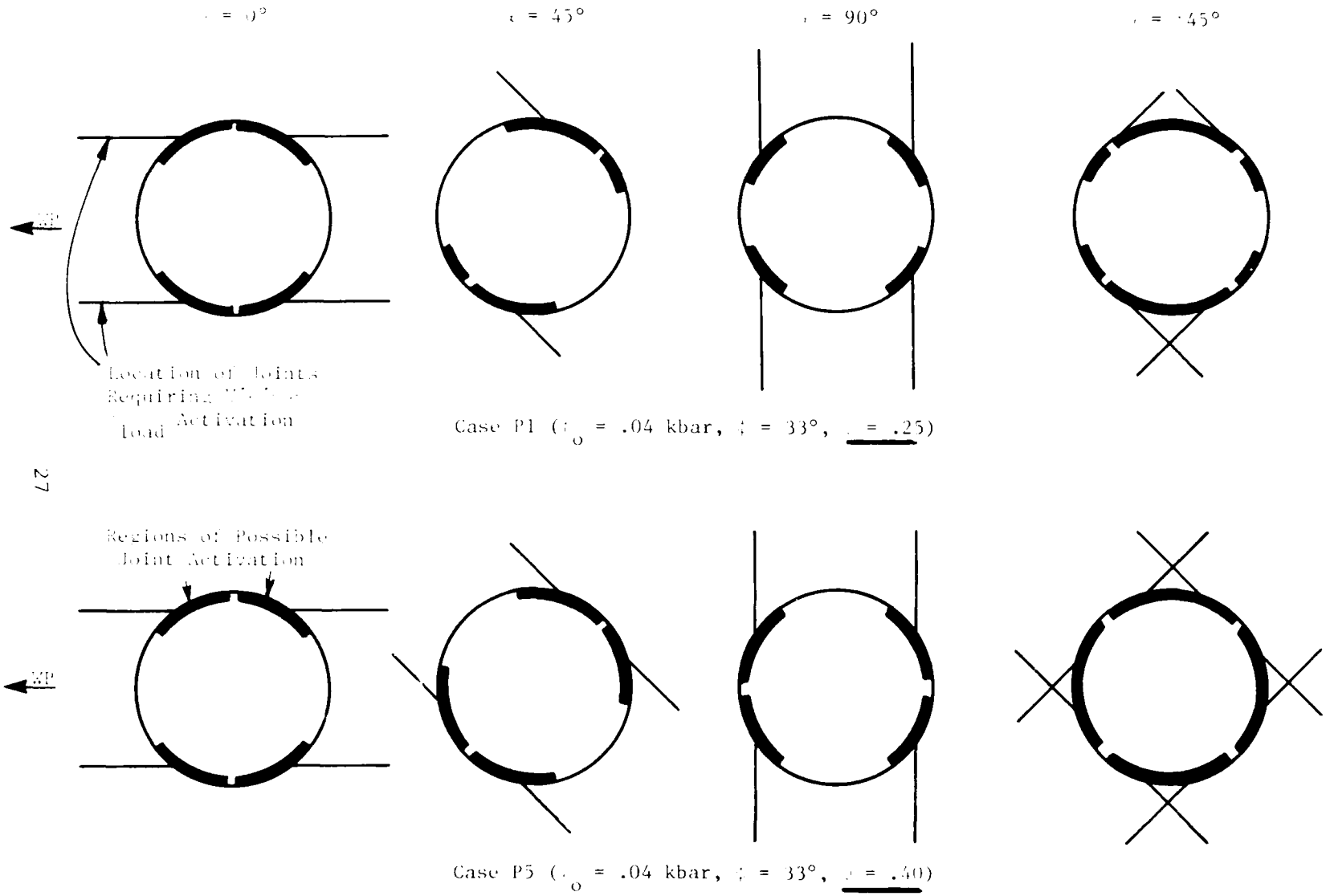

Figure 13. Regions of Possible Joint Activation for a Variation in Poisson's Ratio, ν (σ_{load} = .5 kbar).

Comparisons of the results from the constitutive property cases P1 to P5 leads to the following conclusions:

1. Increasing (or decreasing) the cohesion, τ_o, increases (or decreases) the minimun loading stress for joint activation while leaving unchanged the tunnel angles (β) where joint activation is most likely.

2. Reducing the fiction angle to $\phi = 0$, thereby simulating a von Mises limiting shear strength of τ_o, causes an expansion of the possible joint activation region.

3. Varying Poisson's Ratio for the earth media from $\nu = .25$ to $\nu = .40$ causes an expansion of the possible joint activation region.

SECTION 3

DYNAMIC RESPONSE CASES

In the DIABLO HAWK experiment, the stress wave time history involves rise times to a peak stress of ~0.8 kbars in ~5-10 msec. In Section 4, quasi-static techniques are used to treat this rise

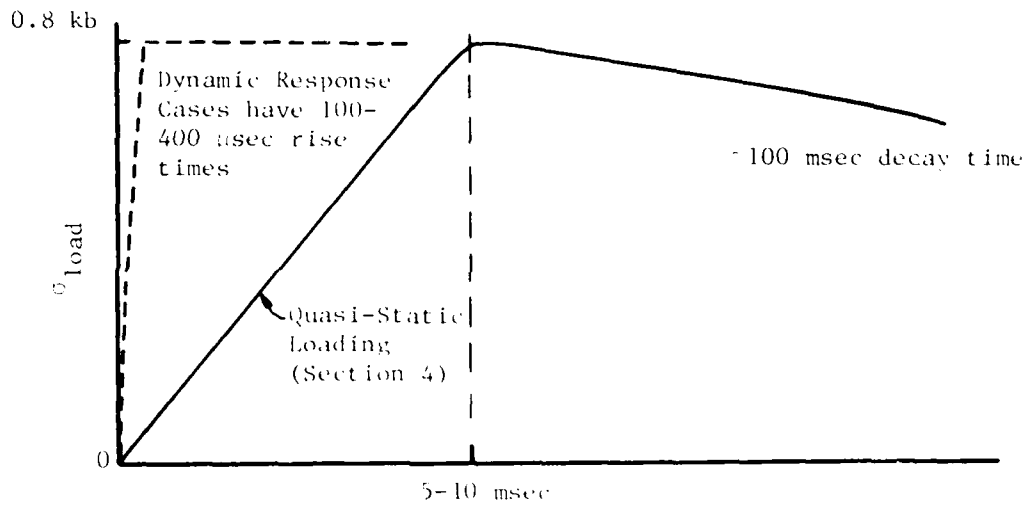

Time After Wave Arrival at 0.8 kbar Stress Range

time, which is quite long with respect to tunnel response. In Section 3.1, material properties for all the cases are described. In Section 3.2, six numerical calculations involving much shorter rise times of between 100 and 400 μsec are described and compared.

3.1 MATERIAL PROPERTIES

16A Rock Simulant

In the small-scale experiments, the jointed media is 16A rock simulant. The elastic-plastic properties are modeled with the following parameters:

Bulk Modulus	$K = .131$ Mbar
Shear Modulus	$G = .086$ Mbar
∴ Poisson's Ratio	$\nu = .23$
Density	$\rho_o = 2.0$ gm/cm^3
Yield Strength	$Y = .22$ kbar + 1.2P, where P is pressure. A Prandtl-Reuss non-associated flow rule is assumed.

Tensile failure is modeled in most of the solutions using a tensile failure model which permits oriented cracks to develop (Ref. 6). A 500 psi = 34.5 bar tensile strength was measured in a simple tensile test (Ref. 7) on a 16A rock simulant sample. Most of our solutions use this value; in one of the cases, the tensile strength is reduced to 6.9 bars (100 psi) as a sensitivity study.

In two of the cases, frictional forces along the sliding joints are included. In these situations the joint constitutive model is specified by:

$$\tau_{max} = \tau_o + \mu\sigma_n = \tau_o + (\tan\phi)\sigma_n$$

where

τ_{max} = maximum allowable shear stress on joint

σ_n = normal stress on joint

τ_o = the joint cohesion

μ = ($\tan\phi$) is the coefficient of friction and ϕ is the angle of friction

The experimental values (Ref. 7) are

τ_o = 10 psi

ϕ = 30°

The Drucker-Prager plastic yield surface assumed for the 16A rock simulant material does not include shear strength softening (i.e., reduction of the yield strength) due to plastic shear deformation or tensile cracking. This may be significant in this application because the uniaxial strain loading path for this material is close to the yield surface. Therefore, small changes in the failure surface may lead to large changes in the plastic response of the 16A rock simulant.

Foam Filler

The tunnel is filled with a low density elastic-plastic foam with the following properties:

Bulk Modulus	K = 1.75 kbar
Shear Modulus	G = 2.5 kbar
Density	ρ_o = .05 gm/cm^3
Von Mises Yield Strength	Y = 500 psi = 0.34 kbar

3.2 CASE COMPARISONS FOR THE 0.8 KBAR DYNAMICALLY LOADED TUNNELS

Table 3 lists the joint geometry, tensile limit, rise time, and material model for the six dynamic loading cases. In all cases the tunnel is filled with low density foam with properties described in Section 3.1.

The loading is a plane wave of 0.8 kbar magnitude. The stress increases linearly from 0 to 0.8 kbar over a characteristic rise time τ_r, (100 μsec in most of these cases). A constant pressure of 0.8 bar is maintained after τ_r. The far-field condition of the pulse (i.e., prior to interaction with the tunnel) is uniaxial strain.

3.2.1 Effect of Loading Rise Time

In the first three cases, the rock media is modeled as an elastic-plastic media with no joints or tensile failure. Cases 1, 2, and 3 differ in their loading rise times (τ_r = 100, 200, and 400 μsec). Cases 4, 5, and 6 have joints which are perpendicular to the wave vector as indicated in Table 3; in these cases, the joint properties and tensile strength of the media are varied.

Figure 14 shows particle velocity (upper part of figure) and principal stress (lower part) fields at 62 μsec for Case 1. Note that the velocity and stress fields have a plane of symmetry which separates the two fields. The scale bars for the velocity vectors and principal stresses are shown on this figure. The following sketch defines the plotting convention for the principal stress:

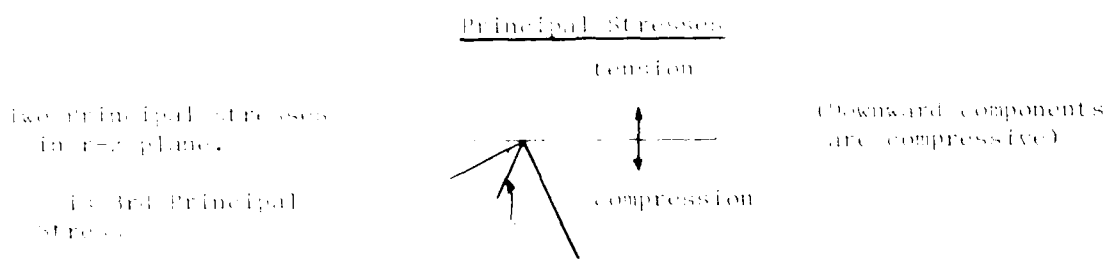

Table 3. The Dynamic Loading Cases

Case	Joints	Tensile Limit	Rise Time τ_r
1	None	None	100 μsec
2	None	None	200 μsec
3	None	None	400 μsec
4	Frictionless ⊥to Wave Vector	100 psi (6.9 bars)	100 μsec
5	Frictionless ⊥to Wave Vector	500 psi (34.5 bars)	100 μsec
6	With Friction (τ_{max} = 10 psi + .6 σ_n) ⊥to Wave Vector	500 psi (34.5 bars)	100 μsec

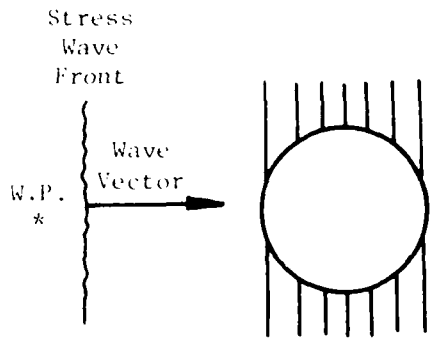

Cases 4, 5, 6

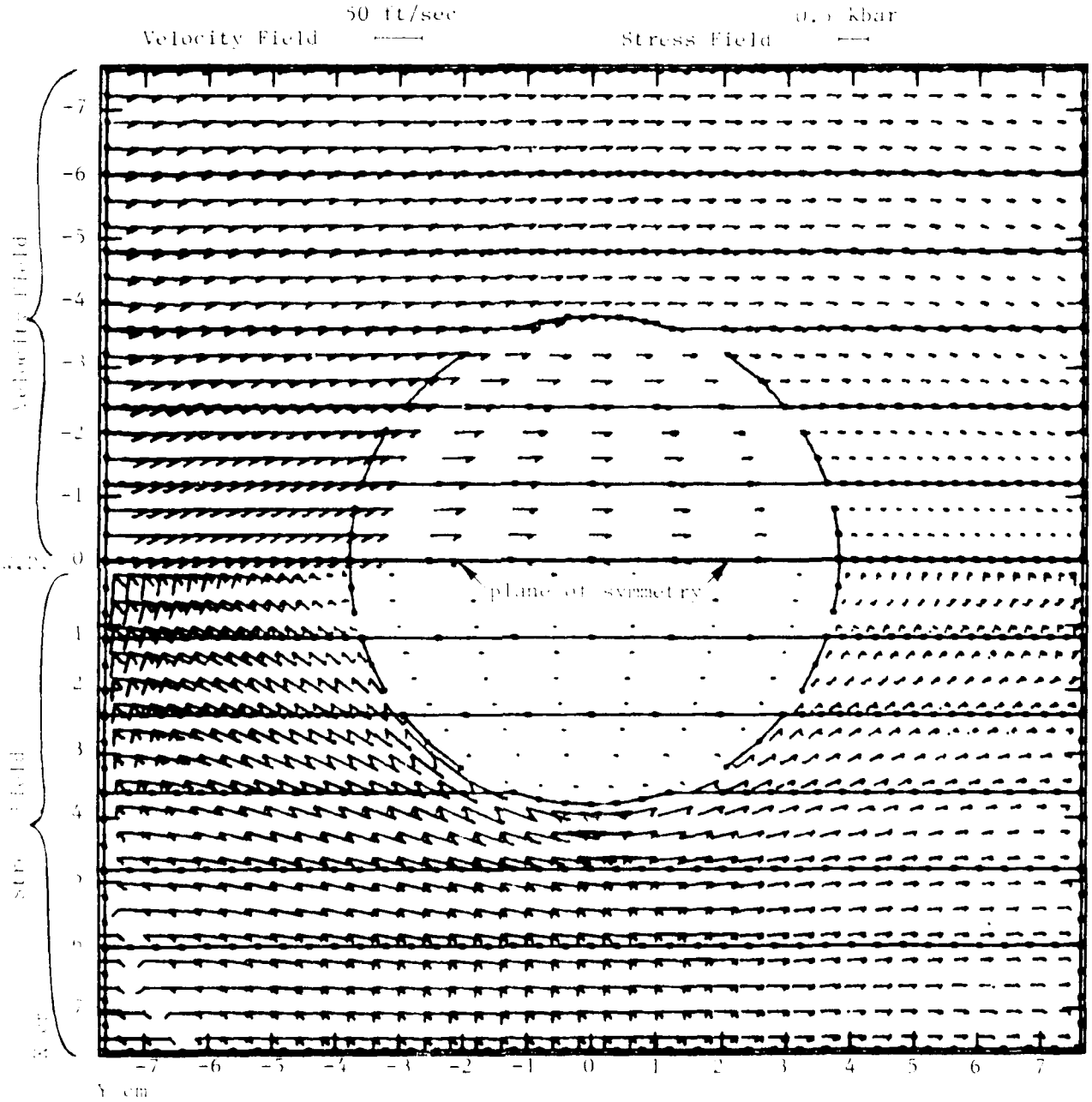

Figure 14. Particle Velocity and Principal Stress Fields at 62 μsec for the Elastic-Plastic Media Model (Case 1, 0.8 kbar Loading in 100 μsec).

The loading wave approaches the tunnel from the left. By 62 μsec, the tunnel is responding very non-symmetrically. Note that one principal stress is nearly zero near the tunnel boundary, and the tangential stress is largest near the springline of the tunnel.

Figure 14 shows that one of the principal stresses is slightly tensile near the tunnel crown (left side of tunnel). Figure 15 shows the tensile stress history at the crown for cases 1, 2, and 3. The tensile response near the crown is clearly dependent on the stress wave rise time for times of a few hundred microseconds and less; a sound wave crosses the characteristic tunnel diameter in about 22 μsec. In the quasi-static solution without joint activation (see Section 4), there was no tensile stress at the crown.

5.2.2 Effects of Rock Tensile Strength and Joint Shear Strength

The WAVE-2 code has the capacity to allow the formation of tensile cracks, to calculate the width of the cracks, and to adjust stresses adjacent to the cracks using elastic stress-strain relationships. After a cell has cracked, no tensile stress across the crack is permitted, and no shear stresses are permitted on the crack if the crack is open (the width of the crack is continuously monitored). These stress adjustments are important because a crack frequently alters the local stress field in such a way as to enhance its own growth; thus, any realistic method of predicting crack growth must consider the altered stress field. Each computational cell is allowed to develop up to two cracks. If a third crack forms, the cell is considered to be completely shattered, and no tension at all is thereafter allowed. The general treatment of tensile failure and the plotting conventions used to indicate the cracked cells in the computational grid plots are illustrated in Figure 16.

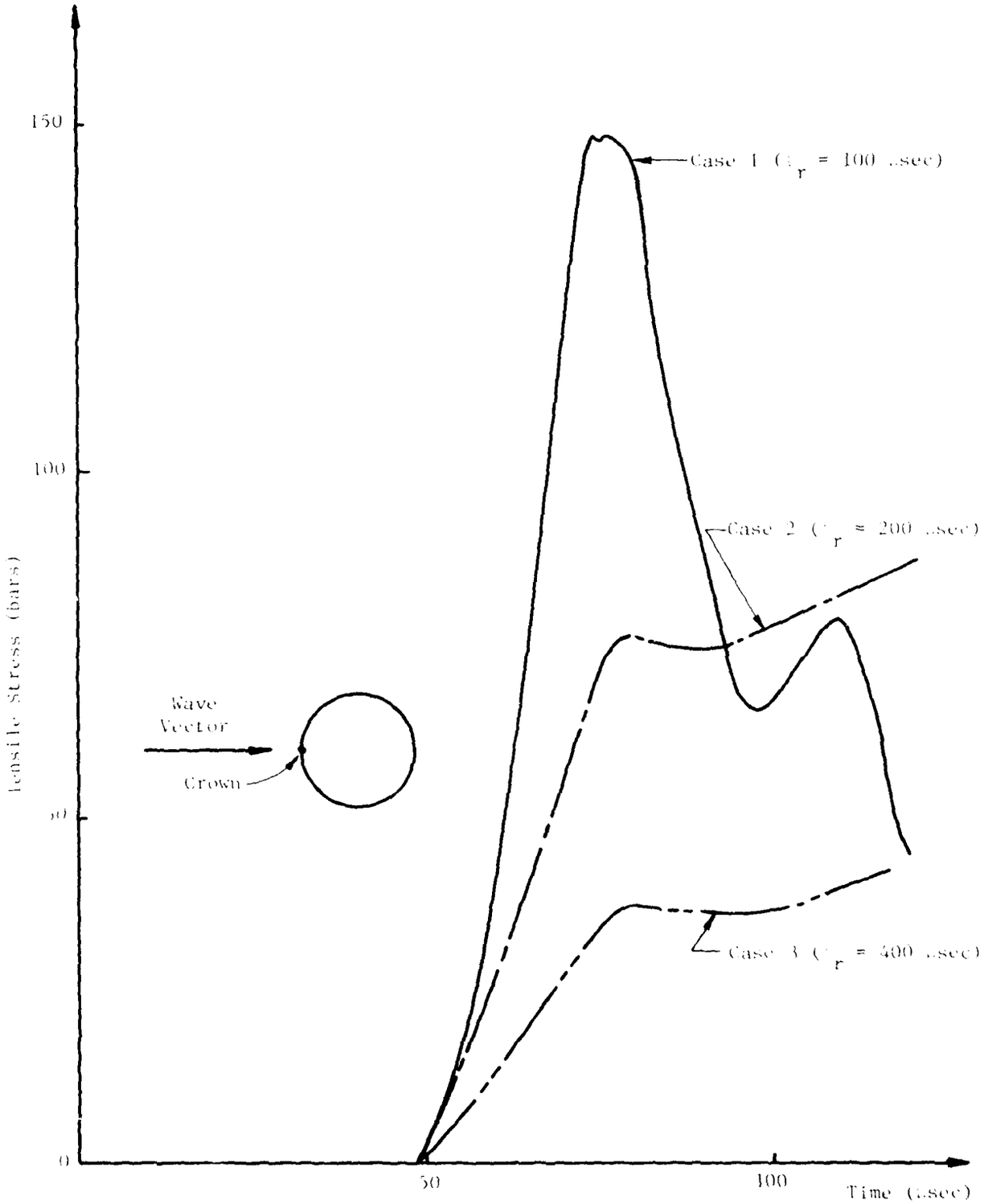

Figure 15. Tensile Stress versus Time at the Tunnel Crown for Various Stress Wave Rise Times (t_r) to a Maximum Load of 0.8 kbar.

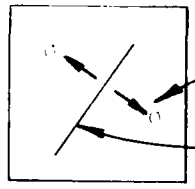

Tensile stresses (σ) exceed the critical tensile failure criterion in the indicated principal stress direction, $\sigma > \sigma_c$

Plane which experiences tensile failure.

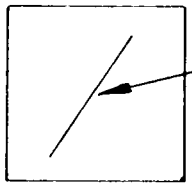

Crack opens and relieves the tensile stress such that no forces or tractions exist on the crack surfaces; i.e., zero normal and shear stress on the crack surface.

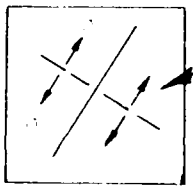

In the directions perpendicular to the crack surface, the material can maintain tensile stresses until the critical tensile failure criterion is exceeded and a new crack is formed.

Plotting Convention:

Single crack in x-y plane. The line is plotted in the direction of the crack (normal to the principal stress causing the crack).

Out-of-plane crack; i.e., $\sigma_{zz} > \sigma_c$ caused the crack.

Out-of-plane and x-y plane crack.

Two x-y plane cracks; only out-of-plane tension is permitted.

Completely fractured - no tension permitted.

Figure 16. Treatment of Tensile Cracks in WAVE-L Code.

In Cases 4 and 5 the sensitivity of the solution to variations in the tensile strength of the rock medium is examined. In Case 4, the 16A rock simulant has a tensile strength of 6.9 bars (= 100 psi); in Case 5, a strength of 34.5 bars (= 500 psi) is used. The effect on the tensile crack formation is shown in Figures 17 and 18 which show these two cases at two different times.

Case 6 implements all the material and joint properties used in the quasi-static DIABLO HAWK simulation (Section 4), including friction along the joints. The presence of the friction is the only difference between Case 5 and 6. The final crack pattern in Case 6 is compared to Case 5 in Figure 19. [illegible]

Tensile cracking of the material near the tunnel surface is closely related to the relative slide displacements across the joints. When slipping occurs across joints, the plates of rock separated by the joints can act as unsupported beams due to the presence of the unlined tunnel. The resulting beam bending leads to tensile stresses and fracture.

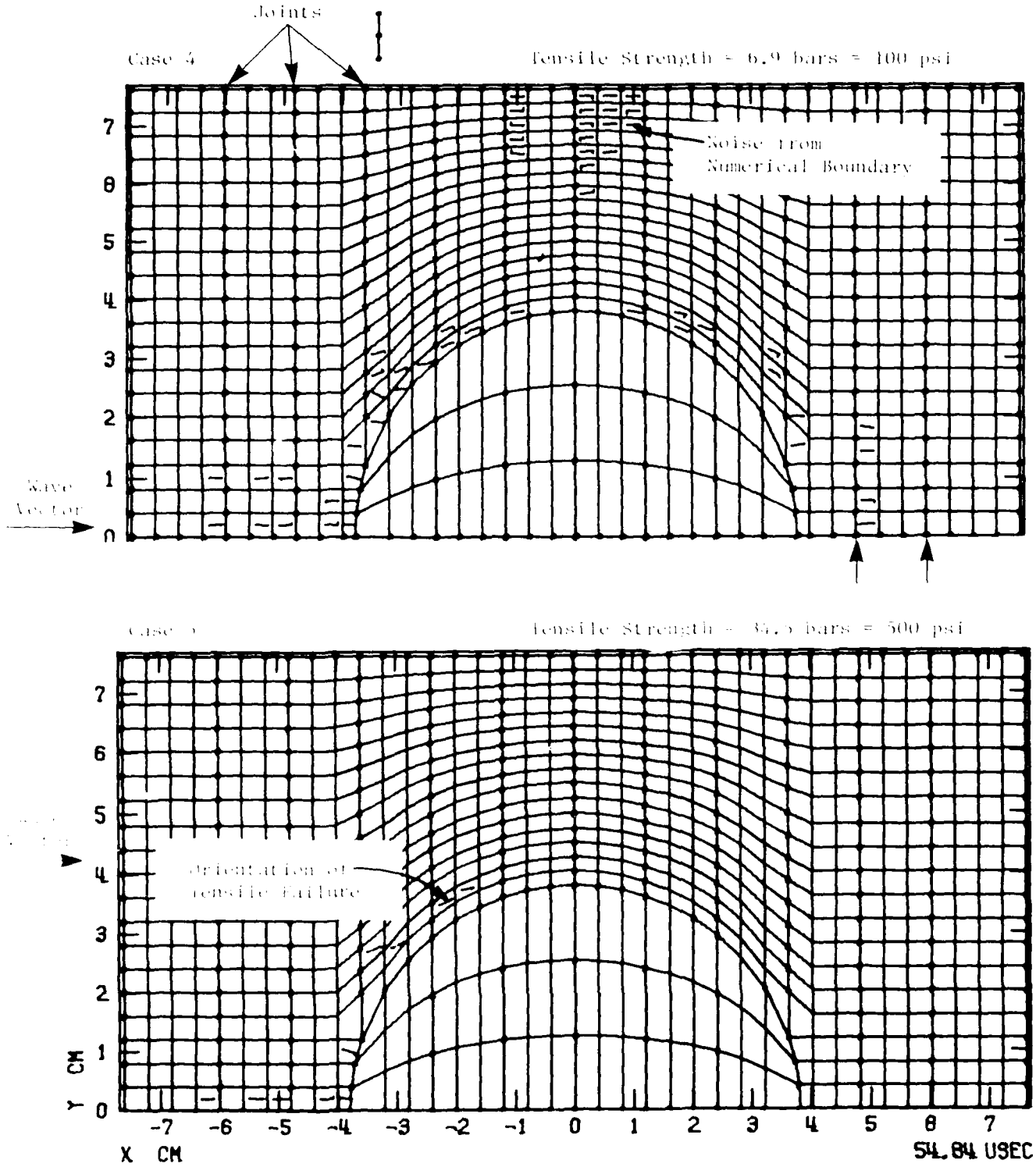

Figure 17. Tensile Crack Configuration at t = 54.84 μsec for Tensile Strength of 100 psi and 500 psi (Cases 4 and 5; 0.8 kbar = 11.6 ksi stress loading in 100 nsec).

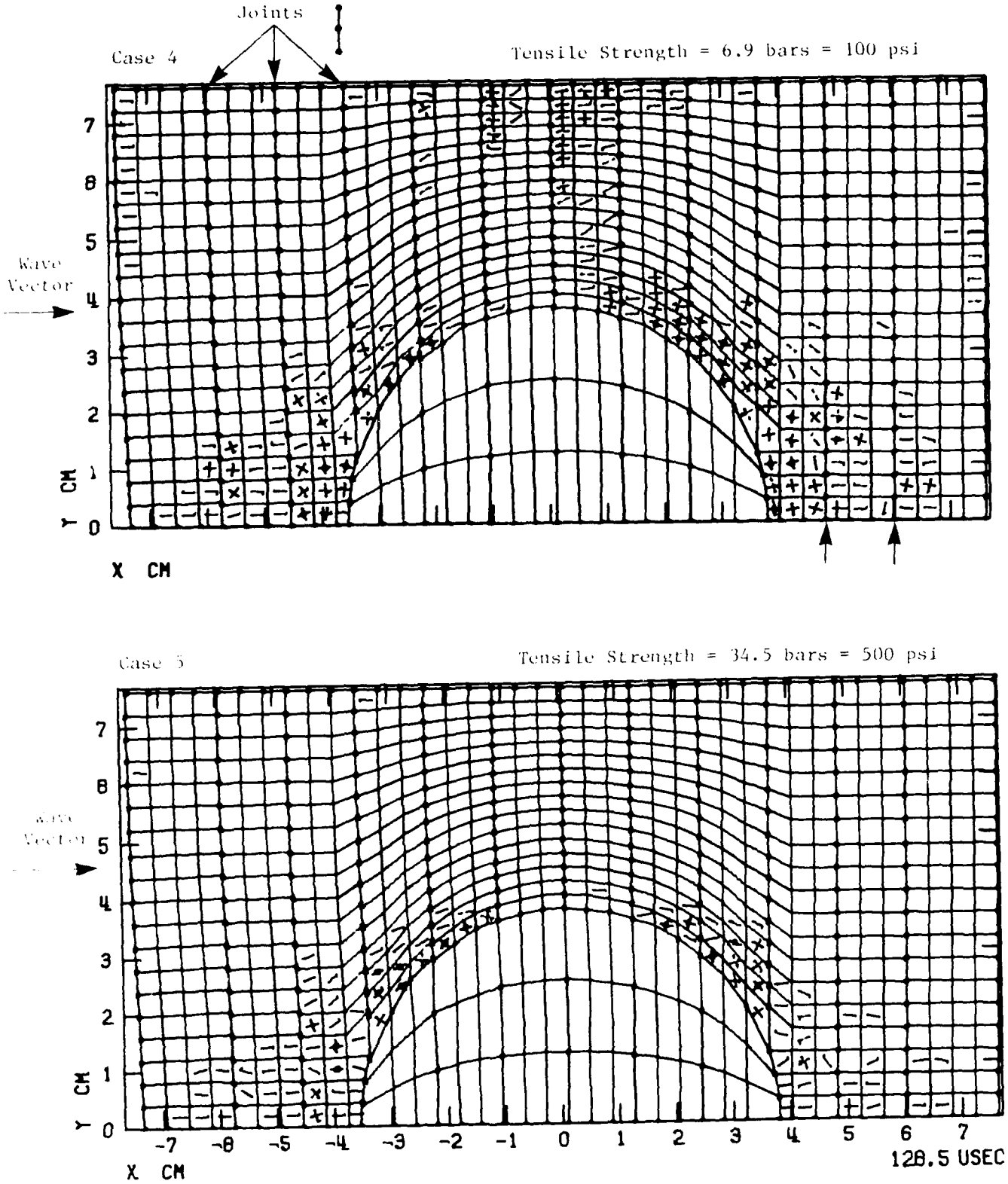

Figure 18. Tensile Crack Configuration at t = 127 μsec for Tensile Strength of 100 psi and 500 psi (Cases 4 and 5; 0.8 kbar = 11.6 ksi Stress Loading in 100 μsec).

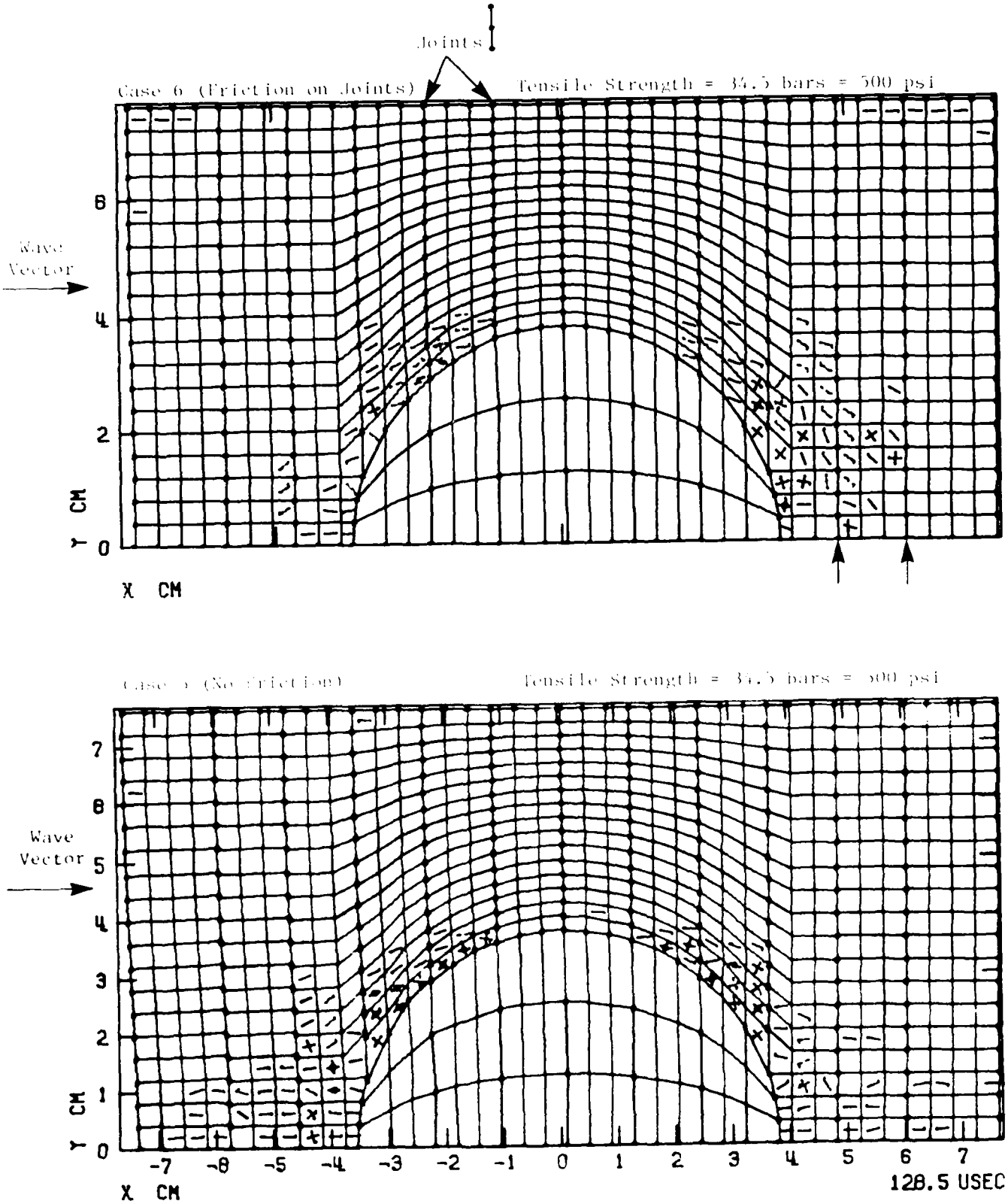

Figure 19. Tensile Crack Configuration at t = 127 μsec for a Variation of Friction (Case 6) versus Frictionless (Case 5) Joints (0.8 kbar = 11.6 ksi Stress Loading in 100 μsec).

SECTION 4

DIABLO HAWK SMALL-SCALE STRUCTURE PREDICTION CASE

This numerical simulation was intended to match a fielded small-scale SRI model. The calculation results were obtained prior to the excavation of the model. The particular model is designated as S-D1-2-5 by SRI.

4.1 PROBLEM CONFIGURATION

The tunnel diameter is 3". Joint spacing is nominally ½" (0.47"). The boundaries of the numerical grid are at 9.45" from the tunnel center (6.3 times the tunnel radius), which is sufficient to minimize edge effects in the region of interest. The joint geometry is shown with the initial computational grid in Figure 20.

Material properties of the 16A rock simulant and foam filler are described in Section 3.1. The frictional properties of the joints are also discussed in that section.

The tunnel and jointed media are subjected to a planar stress wave of 0.8 kbar peak amplitude. The rise time is 5-10 msec and decay 100 msec. These times are very long compared to the 22 μsec sound wave transit time across the tunnel diameter in the 16A material. The actual tunnel, therefore, is in a "quasi-static" state.

4.2 QUASI-STATIC SOLUTION TECHNIQUE

The quasi-static solution is found as indicated on Figure 21:

1. Obtain the elastic solution to a tunnel loaded with the 0.8 kbar (far-field uniaxial strain) stresses.

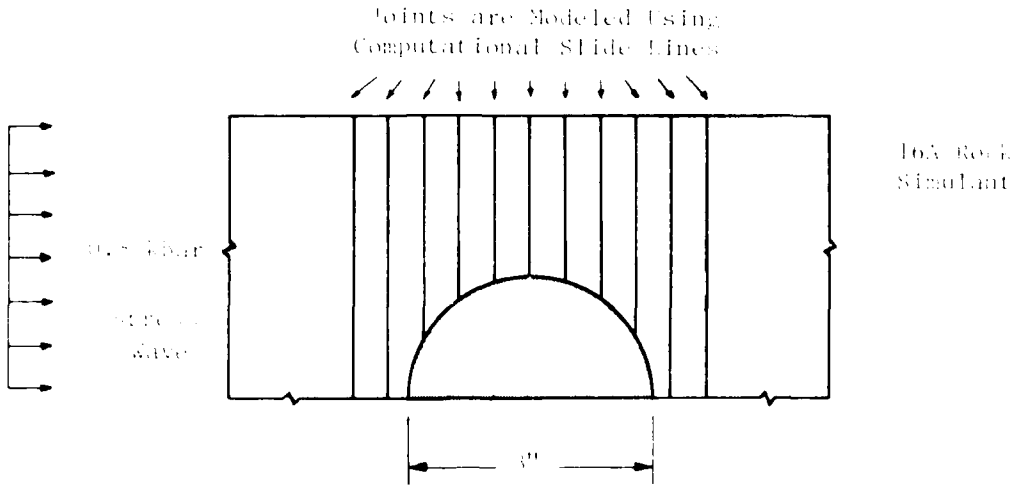

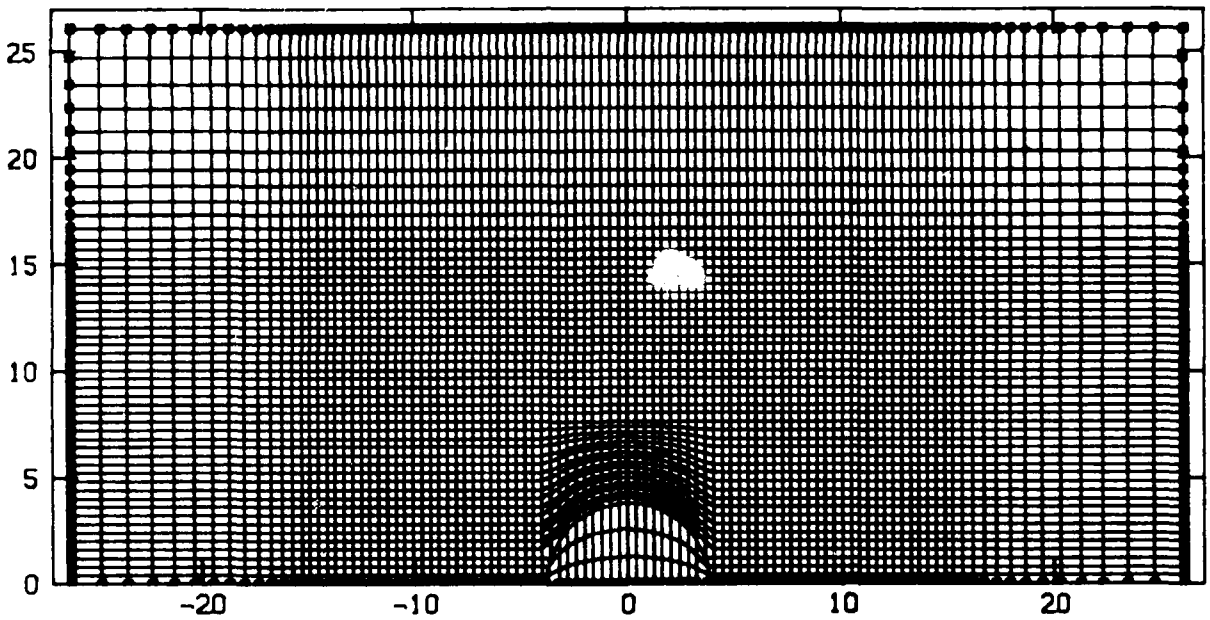

Figure 24. Initial Condition and Computational Grid for the Joints Being Perpendicular to the Wave Vector (Using WES Material Properties).

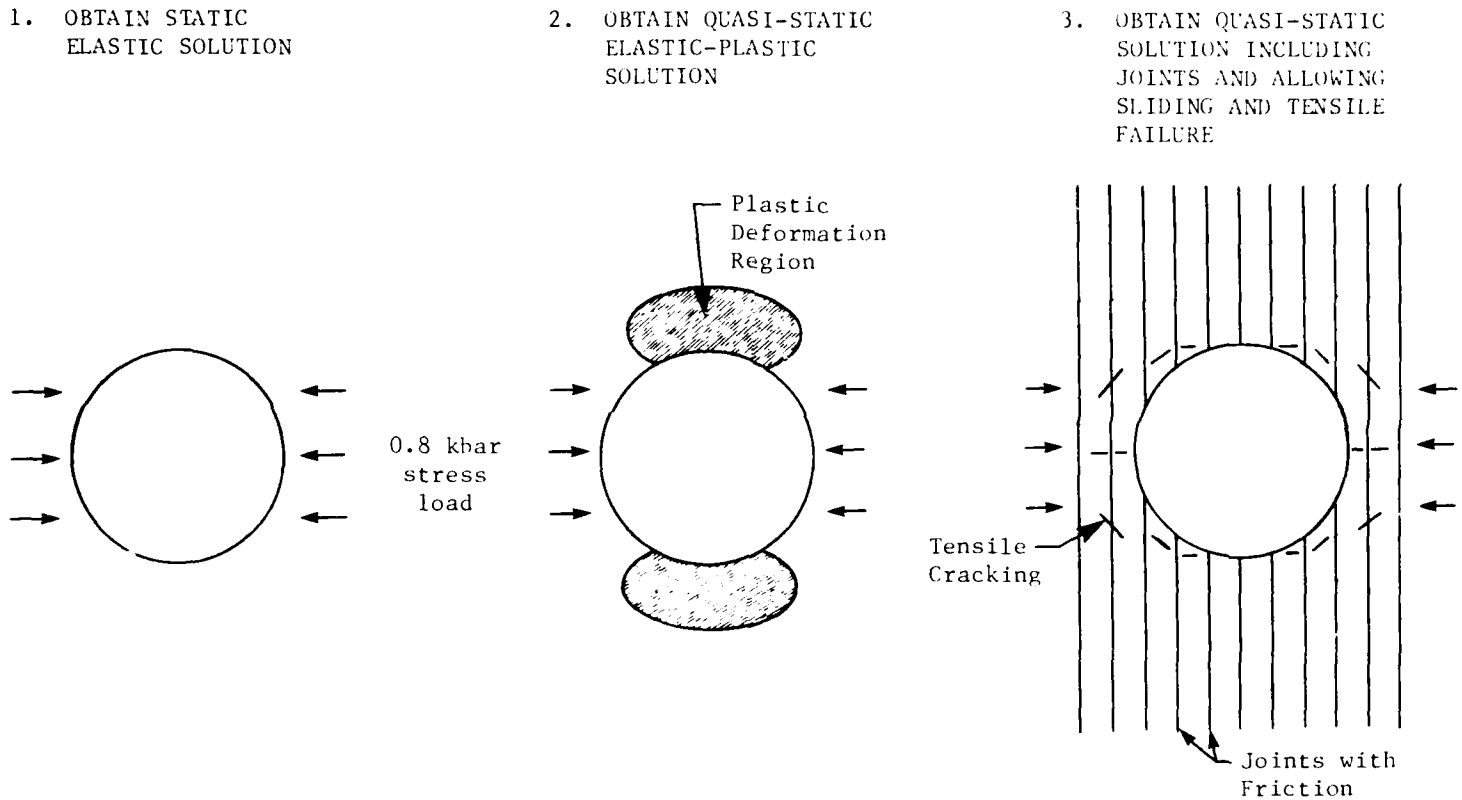

Figure 21. Successive Steps in Quasi-Static Numerical Simulation Technique.

2. Using the elastic solution as initial conditions, activate the elastic-plastic material model and calculate the dynamics until a steady state solution is obtained.

3. Using this elastic-plastic solution as initial conditions, a calculation is performed with the slide lines introduced to model the joints and permit block motion and deformation. Also, the material may fail in tension if the tensile stresses exceed 500 psi in any principal direction. The dynamic calculation is continued until tensile failure, block motion and tunnel deformation have stopped, and a steady-state solution is thereby obtained.

4.3 JOINT SLIDING

Peak slide displacements of 1% of the tunnel diameter are predicted in the quasi-static solution. In a full sized tunnel, with a diameter of 10 feet, this corresponds to 1.2 inches of sliding.

Figure 22 shows the slide displacement along the joint as a function of distance (scaled by tunnel radius) from the tunnel axis. The sliding is a maximum at about one radius along the joints nearest the tunnel crown and invert (Joints 3 and 9 in Figure 22).

4.4 TENSILE CRACKING

The tensile cracking is closely related to the relative slide displacements across the joints. When slipping occurs across a joint, the plates of rock separated by the joints act as beams.

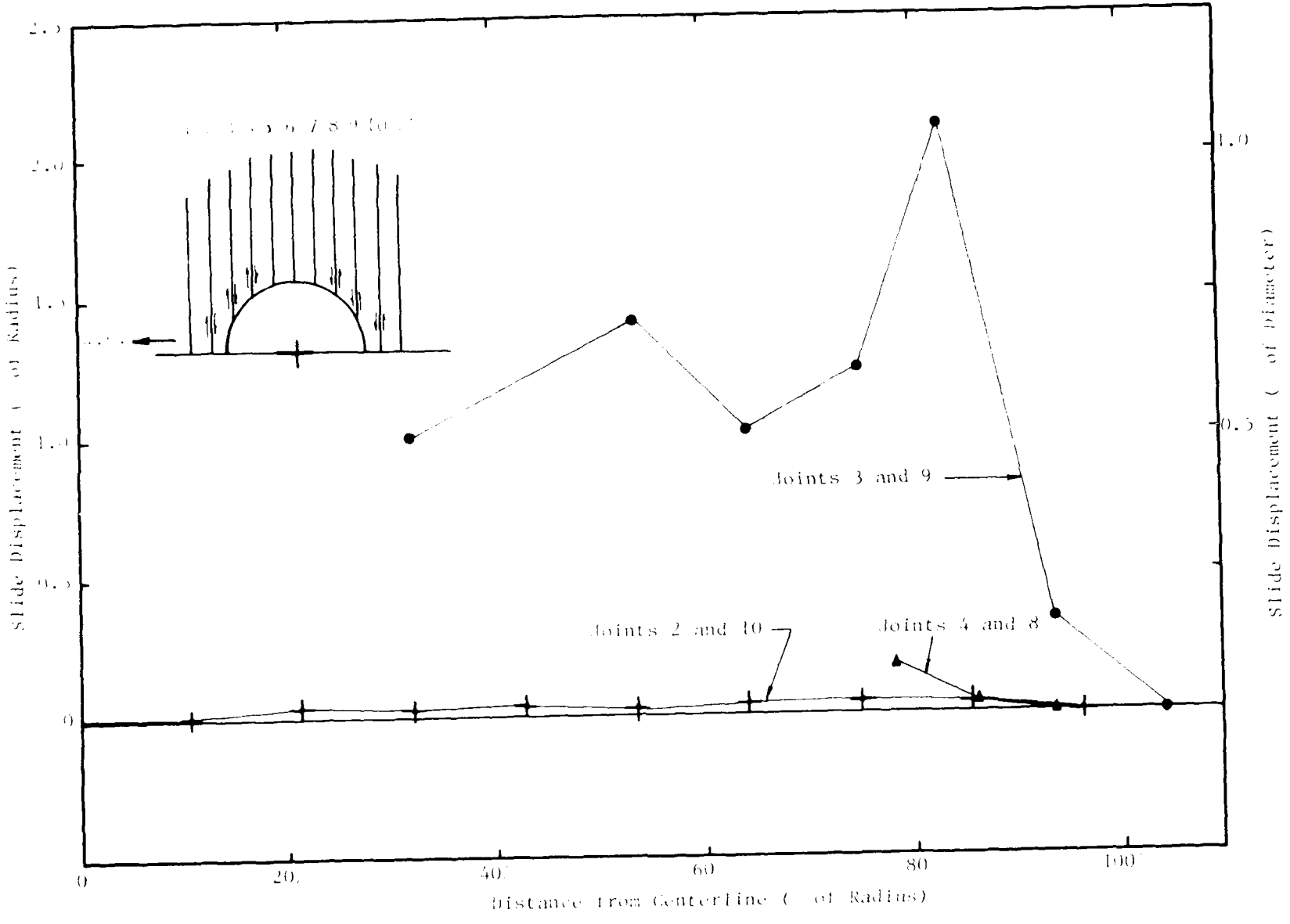

Figure 22. Slide Displacement Along the Various Joints Versus Distance Along the Joint for Quasi-Static Calculation of a Small-Scale Model in DIABLO HAWK.

The presence of the unlined tunnel removes localized support, and beam bending leads to tensile stresses and fracture.

The crack pattern obtained in the numerical solution is shown in Figure 23. The "beams" terminating in the opening show significant cracking of the unsupported cantilevered ends.

4.5 TUNNEL CLOSURE AND COMPARISON WITH EXPERIMENTAL DATA

The tunnel closure predictions are shown on Figure 24. The closure along the vertical axis (i.e., crown-invert) is approximately 0.5%. The maximum closure of 1.2% is located at $\theta = 30°$.

Figure 24 shows a comparison of the actual and predicted tunnel closure (as a % of the diameter) versus tunnel angle. The agreement is quite good except near the crown-invert ($\theta = 0°$ and 180°). The experimental data show a 1.6% closure at the crown-invert compared to a 0.5% predicted value. This difference is probably due to the moderate sliding on the joints and associated tensile failure and relaxation which occurs in the calculations, but not in the experiment.

In the quasi-static calculation, tensile cracking occurs after the joints are "unlocked" and joint sliding begins (see Section 4.4 and Figure 22). Tensile failure is not evident in the post-shot experimental model (Figure 25). If the metal casing (which is not modeled in the calculation) reduced the sliding on the joints, or if the actual joints are stronger (higher cohesion and/or higher coefficient of friction) than used in the calculation, then there would be less block motion in the experiment, and therefore there would also be less tensile failure.

Figure 25 shows the post-shot experimental model. Note the deformation of the thin (.003 inch) metal casing (or liner) surrounding the foam. This casing may have inhibited sliding

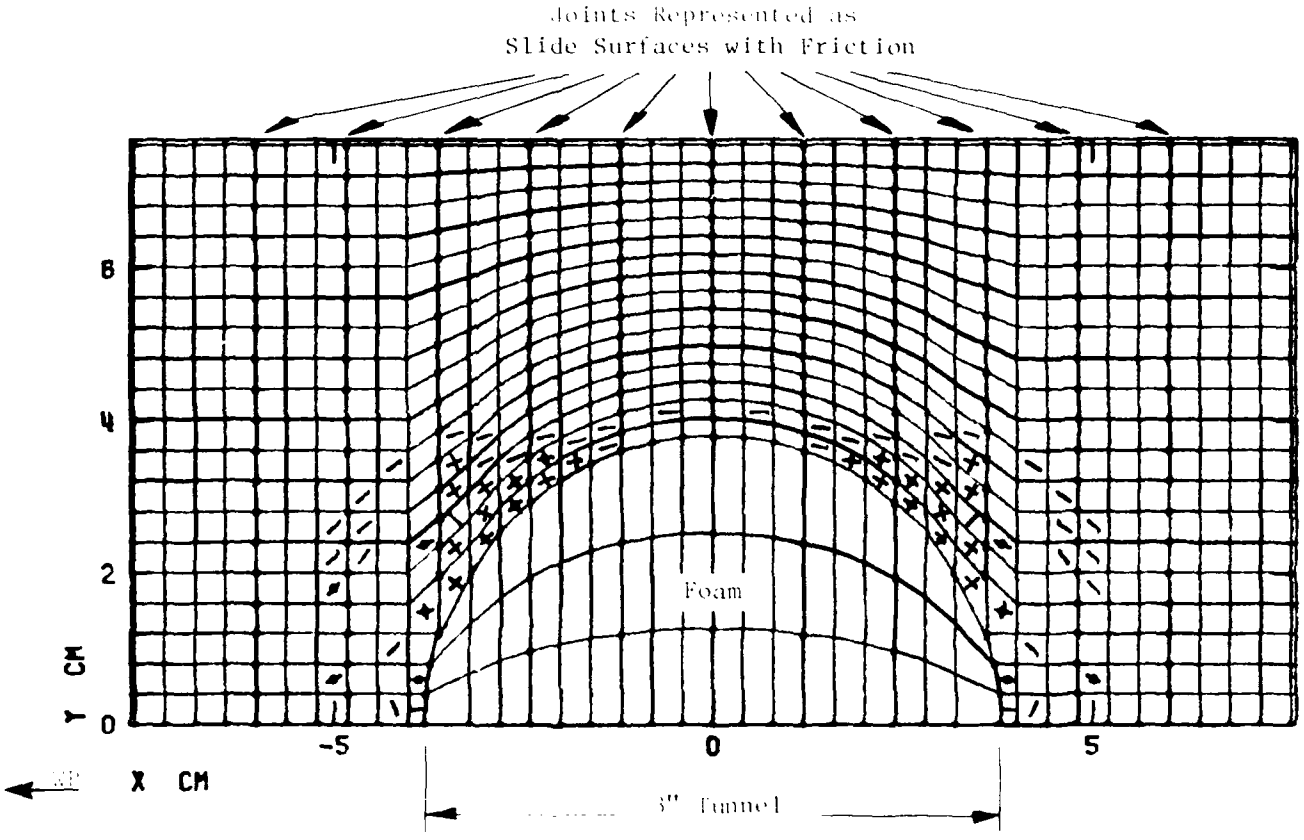

Figure 23. Final Tensile Crack Pattern from Quasi-Static Calculation of Small-Scale Model in DIABLO HAWK.

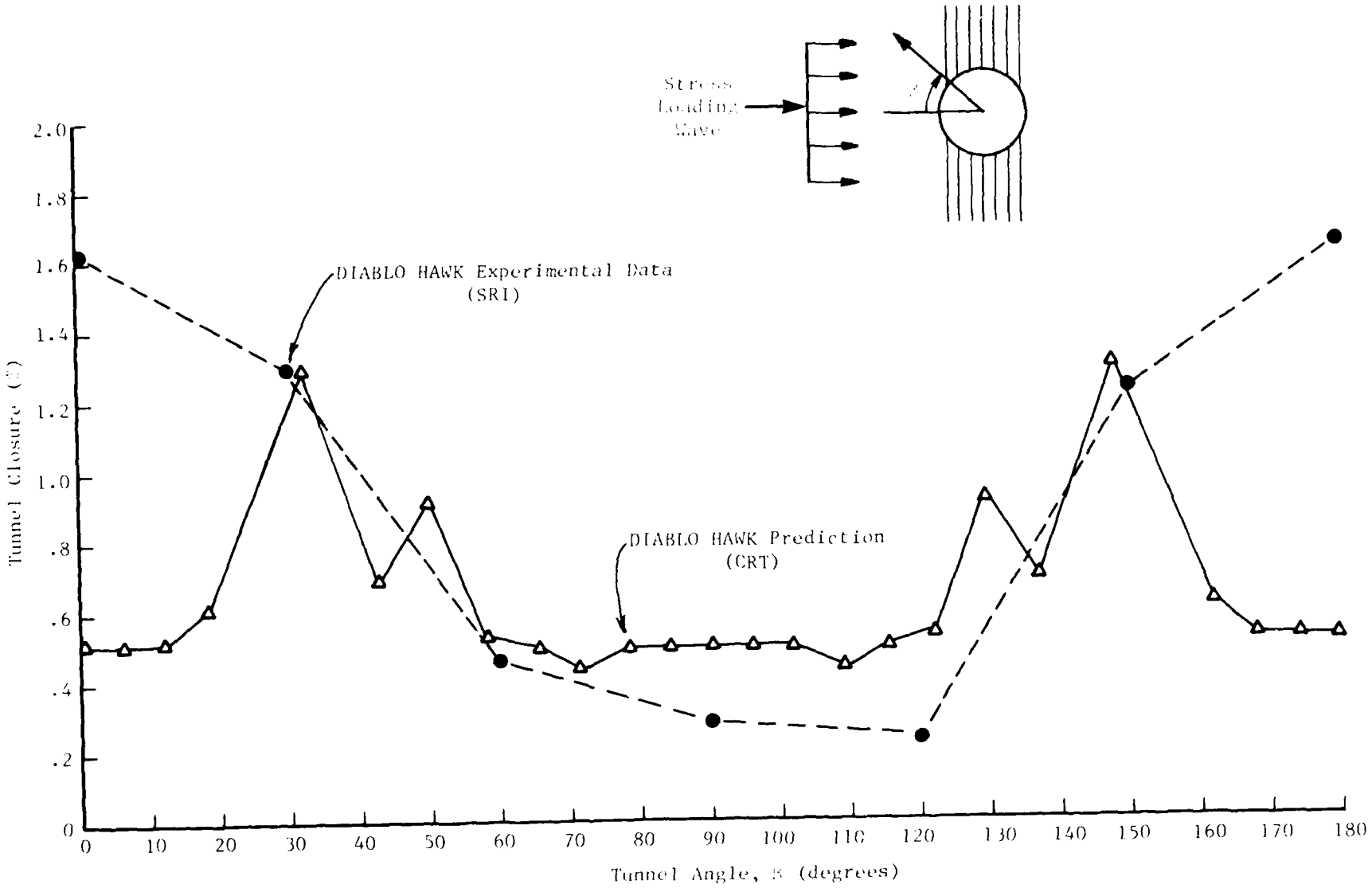

Figure 24. Comparison of Experimental Data and Prediction for the Tunnel Closure ($\frac{\Delta D}{D}$) versus Tunnel Angle for the Small-Scale DIABLO HAWK Model S-D1-2-5.

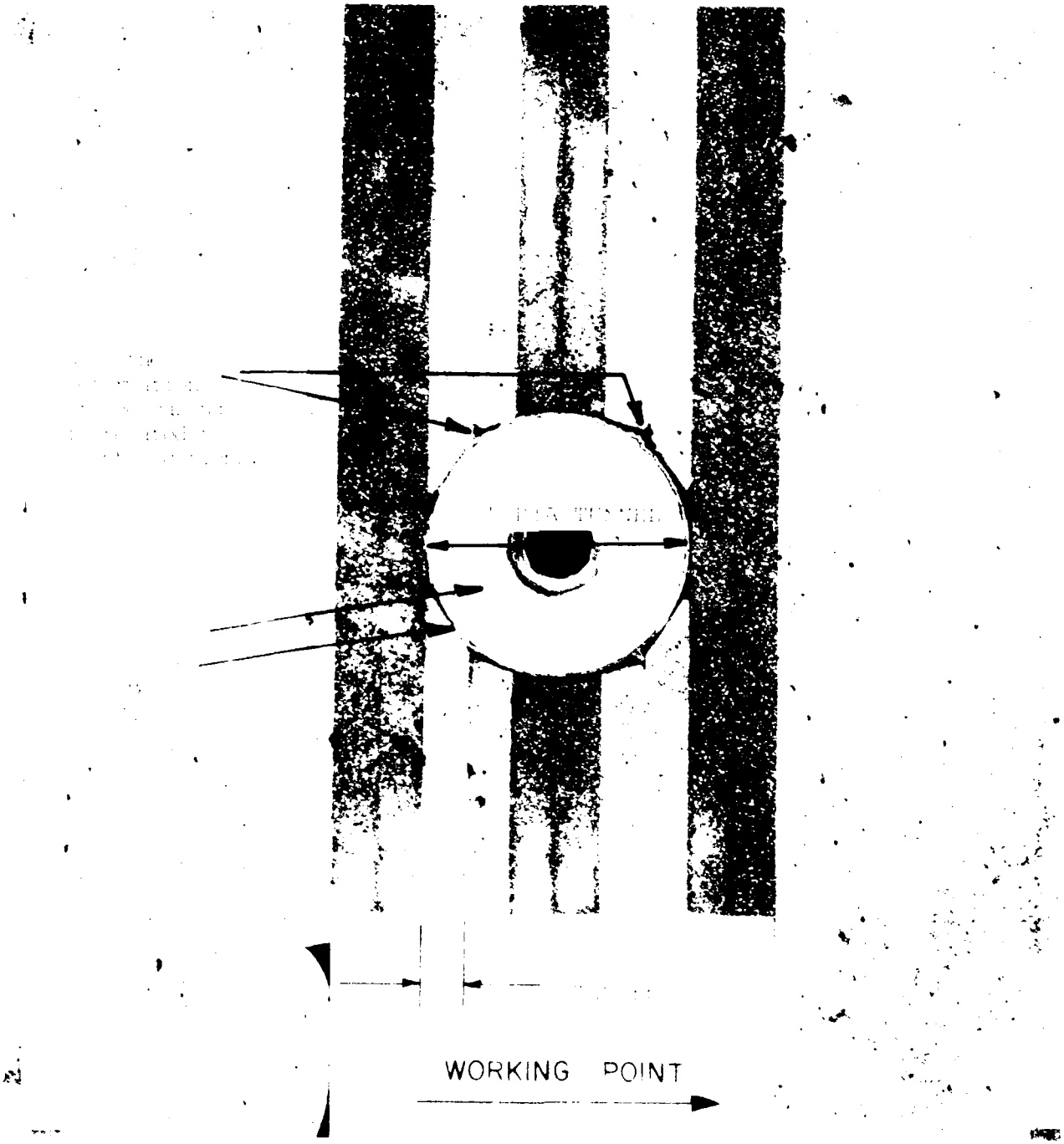

Figure 2-5. Post-Shot Experimental Model S-011-2-5.

along the joints. [illegible] Thus, "block motion" has occurred as predicted. A quantitative description from the small-scale model of the amount of relative displacement across the joints is highly desirable for comparisons with the WAVE-L code predictions of Figure 22.

APPENDIX A

JOINT ACTIVATION CONDITIONS NEAR A CYLINDRICAL TUNNEL

The relationships between the principal stress components (σ_1, σ_2), joint and tunnel angles (α, β), and constitutive activation properties will be obtained using a Mohr diagram (Ref. 8). The joint constitutive model is specified by

$$|\tau|_{max} = \tau_o + \mu\sigma_n$$

or (A-1)

$$|\tau|_{max} = \tau_o + (\tan \phi)\, \sigma_n$$

where

$|\tau|_{max}$ = the maximum allowable shear stress on the joint

σ_n = the normal stress on the joint

τ_o = the joint cohesion

μ = tan ϕ is the coefficient of friction and ϕ is the angle of friction.

Figure A-1 (page 57) is a Mohr diagram which shows (1) the shear stress τ and normal stress σ_n for the joint constitutive model (Equation A-1), and (2) the possible shear and normal stress states corresponding to the principal stresses σ_1 and σ_2. The following sketch (page 54) indicates the geometrical interpretation of the Mohr diagram in terms of the stresses on a joint near a tunnel surface:

PRECEDING PAGE BLANK-NOT FILMED

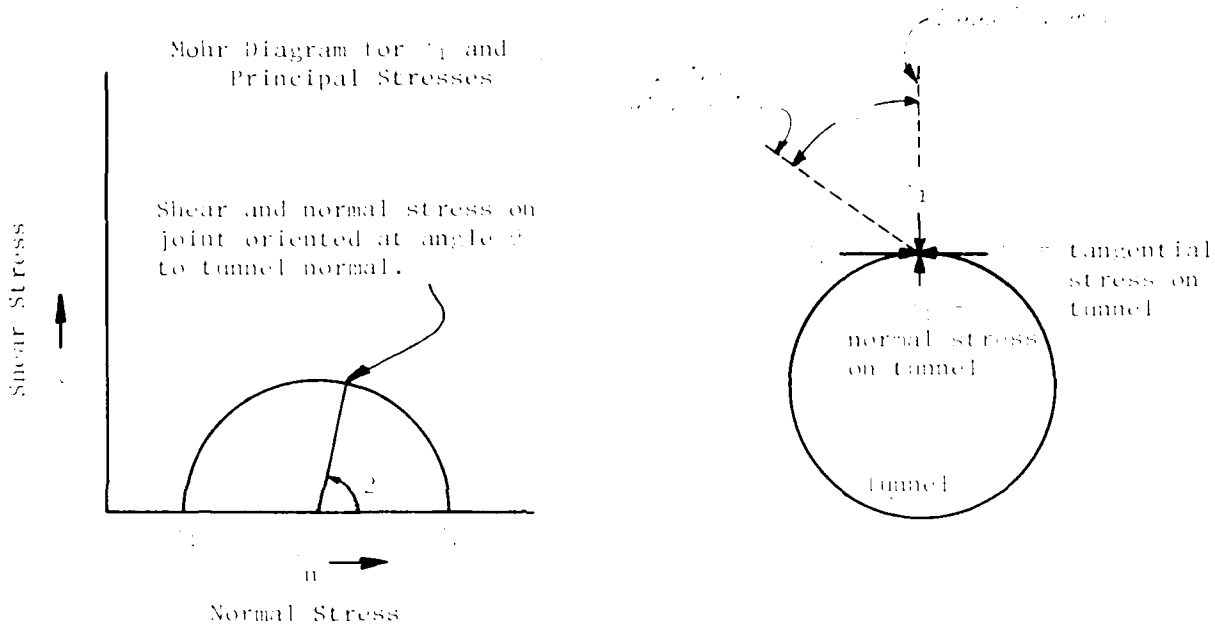

Joint activation will commence when the shear and normal stresses on a joint satisfy the joint constitutive relationship of Equation A-1. Thus, in Figure A-1, the joint activation conditions are satisfied for $\sigma = \sigma_1$ and $\sigma = \sigma_2$. Letting ϕ be the symbol for the critical joint activation angle (either ϕ_1 or ϕ_2), then the geometry of Figure A-1 imples

$$\frac{\sin \phi}{R} = \frac{\sin(2\phi - \phi)}{H}$$

or (A-2)

$$\frac{\sin \phi}{\left(\frac{\sigma_1 - \sigma_2}{2}\right)} = \frac{\sin(2\phi - \phi)}{\left(\frac{\sigma_o}{\mu} + \frac{\sigma_1 + \sigma_2}{2}\right)}$$

Doing the algebra and solving for σ_2, we find,

$$\sigma_2 = \sigma_1\left(\frac{\sin(2\psi-\phi) + \sin\phi}{\sin(2\psi-\phi) - \sin\phi}\right) + \frac{2\tau_o}{\mu}\left(\frac{\sin\phi}{\sin(2\psi-\phi) - \sin\phi}\right) \quad \text{(A-3)}$$

Equation A-3 relates the two principal stresses such that an oriented joint (with angle ψ between the tunnel normal and the joint) will lead to joint activation. A more physical and useful relationship for a plane stress wave engulfing a tunnel can be obtained on a tunnel surface.

On an unlined tunnel surface, one principal stress component vanishes; i.e., $\sigma_1 = 0$. Thus, the tangential stress, σ_2, on the tunnel surface for joint activation is

$$\sigma_2 = \frac{2\tau_o}{\mu}\left(\frac{\sin\phi}{\sin(2\psi-\phi) - \sin\phi}\right) = \frac{2\tau_o\cos\phi}{\sin(2\psi-\phi) - \sin\phi} \quad \text{(A-4)}$$

When a plane wave engulfs a tunnel, however, the tangential st varies with the angle on the tunnel surface as illustrated in the following sketch:

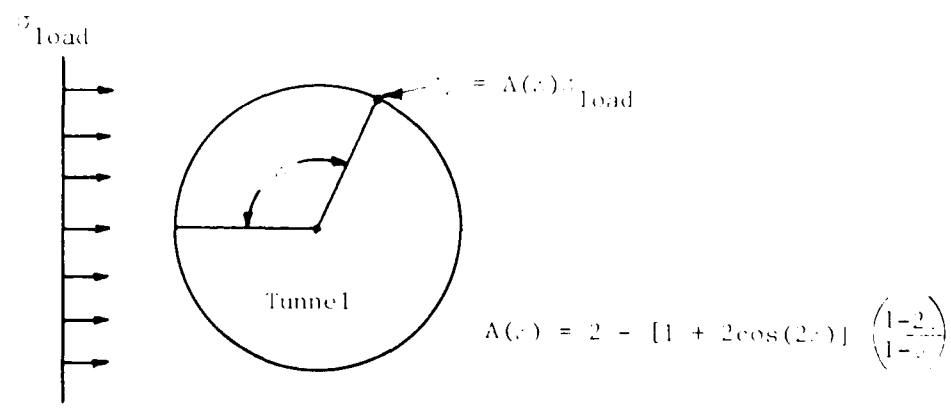

Relationship Between Tangential Stress, σ_t, and Loading Stress, σ_{load}, on Tunnel Surface

In the sketch, $A(\beta)$ is the amplification factor of the σ_{load} wave. $A(\beta)$ depends on the angle β on the tunnel surface and on the elastic Poisson's Ratio (ν) of the media. The derivation for $A(\beta)$ can be obtained by superposition of elastic solutions derived in Reference 8. Figure 5 (in body of report) shows $A(\beta)$ for $\nu = .25$ and $.4$.

Since $\sigma_1 = 0$ and $\sigma_2 = A(\beta)$, σ_{load}, Equation A-4 shows that

$$\sigma_{load} = \frac{\sigma_2}{A(\beta)} = \frac{2\tau_o \cos \phi}{[\sin(2\psi-\phi) - \sin \phi]A(\beta)} \qquad \text{(A-5)}$$

where

$$A(\beta) = 2 - [1 + 2\cos(2\beta)] \frac{1-2\nu}{1-\nu}$$

This is the activation stress load relationship (Equation 1) used in the report.

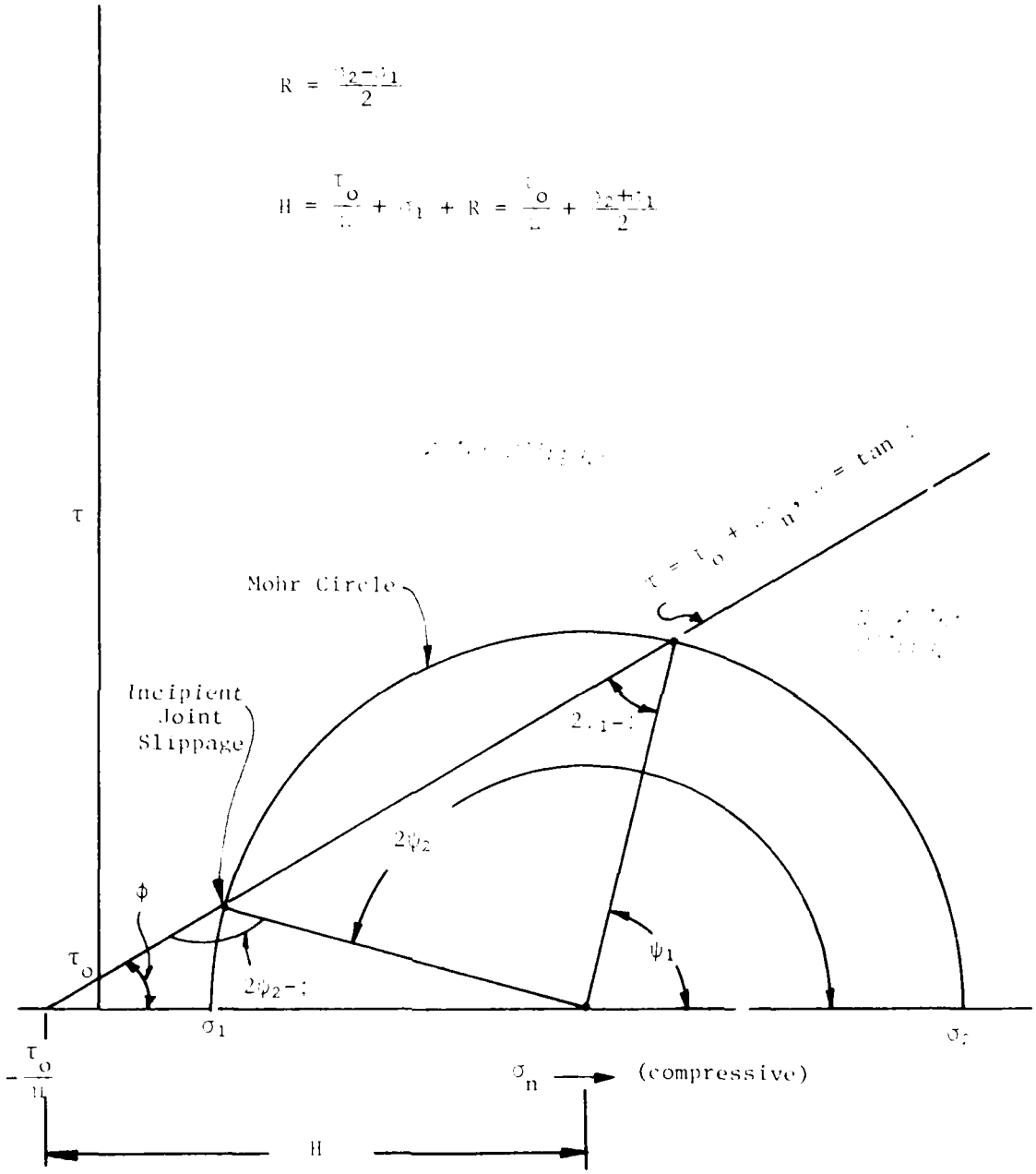

Figure A-1. Mohr Diagram Relating the Shear Stress (τ) and Normal Stress (σ_n) for a Typical Stress State Which Satisfies the Incipient Joint Slippage Criteria at $\theta = \psi_1$ and $\theta = \psi_2$.

REFERENCES

1. S. E. Blouin, "Data Report, DATEX II," AFWL-TR-69-149, January 1970.

2. M. Rosenblatt and K. N. Kreyenhagen, "Free Field Motions in Jointed Media," DNA 2769F, November 1971.

3. M. Rosenblatt, G. E. Eggum, Y. M. Ito and K. N. Kreyenhagen, "Interactions of Stress Waves with Deeply-Buried Tunnels in Geologies with Cracks and Discontinuities," DNA 4398F, June 1975.

4. B. S. Holmes and H. E. Lindberg, "Small-Model Hardened Structures Experiments for Diablo Hawk," SRI77-27, January 1977.

5. M. L. Wilkins, "Calculation of Elastic-Plastic Flow," UCRL-7322, Revision 1, January 1969.

6. M. Rosenblatt, G. E. Eggum, L. A. DeAngelo and K. N. Kreyenhagen, "Numerical Investigation of Water Drop Erosion Mechanisms in Infrared-Transparent Materials," AFML-TR-76-193, December 1976.

7. D. Stowe, Personal Communication, U.S. Army Engineer Waterways Experiment Station, Vicksburg, MS.

8. S. Timoshenko and J. Goddier, Theory of Elasticity, Third Edition, McGraw Hill, 1970.

DISTRIBUTION LIST

DEPARTMENT OF DEFENSE

Assistant to the Secretary of Defense
Atomic Energy
ATTN: Executive Assistant

Defense Intelligence Agency
ATTN: [illegible]
ATTN: [illegible]

Defense Nuclear Agency
ATTN: [illegible]
ATTN: [illegible]
[illegible] ATTN: [illegible]
[illegible] ATTN: [illegible]

Defense Technical Information Center
[illegible] ATTN: [illegible]

Field Command
Defense Nuclear Agency
ATTN: [illegible]
ATTN: [illegible]

Field Command
Defense Nuclear Agency
[illegible]
ATTN: [illegible]

Field Command Test Directorate
Defense Nuclear Agency
[illegible] ATTN: [illegible]

[illegible]
ATTN: [illegible]
ATTN: [illegible] Library

[illegible]
ATTN: [illegible]

[illegible]

[illegible]
[illegible]
ATTN: [illegible]
ATTN: [illegible]

[illegible]
[illegible]
ATTN: [illegible]

[illegible]
[illegible]
ATTN: [illegible]

[illegible]
ATTN: [illegible]
ATTN: [illegible]
ATTN: [illegible]
ATTN: [illegible]

[illegible]
ATTN: [illegible]

DEPARTMENT OF THE ARMY (Continued)

U.S. Army Concepts Analysis Agency
ATTN: [illegible]

U.S. Army Engineer Center
ATTN: [illegible]

U.S. Army Engineer [illegible]
ATTN: [illegible]

U.S. Army Engineer [illegible]
ATTN: [illegible]
ATTN: [illegible]

U.S. Army Engineer [illegible]
ATTN: [illegible]

U.S. Army Engineer Waterways Experiment Station
ATTN: [illegible]
ATTN: [illegible]
ATTN: [illegible]
ATTN: [illegible]
ATTN: [illegible]
ATTN: Library
ATTN: [illegible]
ATTN: [illegible]

U.S. Army Nuclear & Chemical Agency
ATTN: Library

DEPARTMENT OF THE NAVY

Chief of Naval Operations
Department of the Navy
ATTN: [illegible]

Naval Construction Battalion Center
ATTN: Code [illegible]

Naval Electronic System Command
ATTN: [illegible]

Naval Postgraduate School
ATTN: Code 1424, Library

Naval Research Laboratory
ATTN: Code [illegible]

Naval Surface Weapons Center
ATTN: Tech Lib & Info Svcs Branch

Naval War College
ATTN: Code [illegible]

Strategic Systems Project Office
Department of the Navy
ATTN: [illegible]

DEPARTMENT OF THE AIR FORCE

Air Force Institute of Technology
Air University
ATTN: Library

DEPARTMENT OF THE AIR FORCE (Continued)

Air Force Weapons Laboratory
Air Force Systems Command
ATTN: NTE, M. Plamondon
ATTN: NT, D. Payton
ATTN: SUL

Air University Library
Department of the Air Force
ATTN: AUL/LSE

Assistant Chief of Staff
Studies & Analyses
Department of the Air Force
ATTN: AF/SASM
ATTN: AF/SASM, W. Adams

Ballistic Missile Office
Air Force Systems Command
ATTN: MNN
ATTN: MNNH

Deputy Chief of Staff
Operations Plans and Readiness
Department of the Air Force
ATTN: AFXODC

Deputy Chief of Staff
Research, Development, & Acq
Department of the Air Force
ATTN: AFRDQI

Foreign Technology Division
Air Force Systems Command
ATTN: TDIS Library

Strategic Air Command
Department of the Air Force
ATTN: XPFS
ATTN: NRI-STINFO Library

OTHER GOVERNMENT AGENCIES

Central Intelligence Agency
ATTN: OSWR/NED

Department of the Interior
Bureau of Mines
ATTN: Tech Lib

Department of the Interior
U.S. Geological Survey
ATTN: R. Carroll
ATTN: W. Twenhofel

Department of the Interior
U.S. Geological Survey
ATTN: D. Roddy

DEPARTMENT OF ENERGY CONTRACTORS

Lawrence Livermore National Lab
ATTN: Technical Info Dept Library
ATTN: L-21, D. Oakley
ATTN: G. Smith
ATTN: H. Heard

Oak Ridge National Laboratory
ATTN: Central Research Library

DEPARTMENT OF ENERGY CONTRACTORS (Continued)

Los Alamos National Scientific Lab
ATTN: B. Killian
ATTN: J. Johnson
ATTN: MS 364
ATTN: L. Germaine

Sandia Laboratories
Livermore Laboratory
ATTN: Library & Security Classificatior Div.

Sandia National Lab
ATTN: L. Hill
ATTN: 3141

DEPARTMENT OF DEFENSE CONTRACTORS

Aerospace Corp.
ATTN: P. Mathur
ATTN: Technical Information Services

Agbabian Associates
ATTN: M. Balachanda
ATTN: C. Bagge
2 cy ATTN: M. Agbabian

Applied Theory, Inc.
2 cy ATTN: J. Trulio

AVCO Research & Systems Group
ATTN: Library A830

BDM Corp.
ATTN: Corporate Library
ATTN: T. Neighbors

Boeing Co.
ATTN: T. Berg
ATTN: R. Dyrdahl
ATTN: M/S 42/37, K. Friddell
ATTN: H. Leistner
ATTN: Aerospace Library
ATTN: J. Wooster

California Institute of Technology
ATTN: D. Anderson

California Research & Technology, Inc.
ATTN: Library
ATTN: S. Schuster
ATTN: K. Kreyenhagen
4 cy ATTN: M. Rosenblatt
4 cy ATTN: L. DeAngelo

California Research & Technology, Inc.
ATTN: D. Orphal

University of California
ATTN: N. Cook
ATTN: R. Goodman

Calspan Corp
ATTN: Library

University of Denver
ATTN: J. Wisotski

EG&G Wash Analytical Svcs Ctr, Inc.
ATTN: Library

DEPARTMENT OF DEFENSE CONTRACTORS (Continued)

Electromech Sys of New Mexico, Inc
ATTN: R. Shunk

University of New Mexico
Civil Engineering Rsch Fac
ATTN: N. Baum

Foster-Miller Associates, Inc
ATTN: J. Hampson for E. Foster

Franklin Institute
ATTN: Z. Zudans

IIT Research Institute
ATTN: M. Johnson
ATTN: R. Welch
ATTN: Documents Library

Institute for Defense Analyses
ATTN: Classified Library

J. H. Wiggins Co, Inc
ATTN: J. Collins

Kaman AviDyne
ATTN: Library

Kaman Sciences Corp
ATTN: Library

Kaman TEMPO
ATTN: DASIAC

J. D. Haltiwanger Consult Svcs
ATTN: J. D. Haltiwanger

Lockheed Missiles & Space Co, Inc
ATTN: Technical Information Center
ATTN: T. Geers

Massachusetts Inst of Technology
ATTN: W. Brace

Merritt Cases, Inc
ATTN: J. Merritt

City College of New York
ATTN: [illegible] Miller

Northwestern University
ATTN: T. Belytschko

Pacific-Sierra Research Corp
ATTN: H. Brode

Pacific-Sierra Research Corp
ATTN: D. Gormley

Pacifica Technology
ATTN: G. Kent

Patel Enterprises, Inc
ATTN: M. Patel

Physics International Co
ATTN: E. Moore
ATTN: Technical Library
ATTN: F. Sauer

DEPARTMENT OF DEFENSE CONTRACTORS (Continued)

R & D Associates
ATTN: D. Rawson
ATTN: D. Shrinivasa
ATTN: R. Port
ATTN: J. Lewis
ATTN: Technical Information Center
ATTN: P. Haas

Rand Corp
ATTN: A. Laupa

Science Applications, Inc
ATTN: Technical Library

Science Applications, Inc
ATTN: Technical Library

Science Applications, Inc
ATTN: W. Layson

Southwest Research Institute
ATTN: A. Wenzel
ATTN: W. Baker

SRI International
ATTN: G. Abrahamson
ATTN: H. Lindberg
ATTN: B. Holmes

Systems, Science & Software, Inc
ATTN: R. Duff
ATTN: C. Archembeam
ATTN: Library
ATTN: D. Grine

Terra Tek, Inc
ATTN: H. Pratt
ATTN: Library

Texas A & M University System
ATTN: A. Rychlik
ATTN: J. Handin

TRW Defense & Space Sys Group
ATTN: P. Huff
ATTN: Technical Information Center
ATTN: N. Lipner

TRW Defense & Space Sys Group
ATTN: E. Wong
ATTN: P. Dai

Universal Analytics, Inc
ATTN: E. Field

Weidlinger Associates, Consulting Engineers
ATTN: M. Baron
ATTN: I. Sandler

Weidlinger Associates, Consulting Engineers
ATTN: J. Isenberg

William Perret
ATTN: W. Perret

DATE
FILMED

-8